Study of the morphology control and solid solution behaviour of Olivine $LiMPO_4$ (M = Fe, Mn, and Co)

by

Wang Hay Kan

A thesis

presented to the University of Waterloo

in fulfillment of the

thesis requirement for the degree of

Master of Science

in

Chemistry

Waterloo, Ontario, Canada, 2009

I hereby declare that I am the sole author of this thesis.

This is a true copy of the thesis, including any required final revisions, as accepted by my examiners.

I understand that my thesis may be made electronically available to the public.

Abstract

Lithium iron phosphate ($LiFePO_4$) is one of the most promising cathode materials for lithium ion rechargeable batteries. It has a high theoretical specific capacity (170 mAh/g) and operating potential (3.45 V vs. Li^+/Li). Additionally, the material is extremely stable thermally and electrochemically at ambient conditions, which is very suitable to be used in electric vehicles. However, the electronic and ionic conductivities of the material are quite low, which limits the power performance of the batteries. In the last decade, extensive work was reported on various methods to improve the electronic conductivity extrinsically, for example carbon coating, metallic additives and molecular wiring. Nevertheless, energy density of the cells will be reduced because of non-electrochemically active nature of the additives. In principle, electronic and ionic conductivities can be boosted intrinsically. One of the methods is to increase the number of charge carriers in the material, for instance in two-phase solid solution system $Li_\alpha FePO_4/Li_{1-\beta}FePO_4$ or single solid solution phase Li_xFePO_4. Since the formation of solid solution has been reported to be size dependent, it is highly desired to know how to synthesize $LiFePO_4$ particles with different sizes. In this study, we have used hydrothermal synthesis and polyol process to control the size of $LiMPO_4$ (M: Fe, Mn, and Co) particles. We will present how we prepare particles with different sizes. Moreover, the solid solution properties of various sizes of $LiMPO_4$ (M: Mn and Fe) were studied. The result will be presented.

Part of the preliminary findings have been published in the peer-reviewed journals or conference presentations: 1) Journal of Materials Chemistry [Ellis B.; Kan W. H.; Makahnouk W. R. M.; Nazar L. F. *J. Mater. Chem.* **2007**, 17 (30) 3248., 2) Journal of the American

Chemical Society [Lee K. T.; Kan W. H.; Nazar L. F. *J. Am. Chem. Soc.* DOI: 10.1021/ja8090559, 3) Material Research Society Meeting [Kan W. H.; Maunders C.; Badi S.; Ellis B.; Botton G.; Nazar L. F. MRS Fall Meeting 2008 in Boston]

Acknowledgements

This thesis could not be done without many help from people around me. First of all, I thank my supervisor, Prof. Linda F. Nazar, who provided me an opportunity to study solid state and electrochemical chemistry on lithium cathode materials. Her dedication to explore the nature of materials has influenced me to do research cautiously. I appreciate her help on my master study.

I thank my research committee members, Prof. Holger Kleinke and Prof. Sonny Lee for their time and advice during my study.

I thank Prof. Gianluigi Botton and Dr. Christian Maunders for TEM measurements in McMaster University. I thank Prof. Tong Leung and his group members for SEM measurements in Watlab in University of Waterloo.

I thank the current and former group members: Dr. Kyutae Lee, Dr. Shriprakash Badi, Dr. Ramesh Thimmasandra Narayan, Dr. Yasutosho Iriyama, David Ji, Antony Han, Jim Chung, Brian Ellis, Sihyoung Oh, Guang He, Rajesh Tripathi, and others.

Table of Contents

List of Figures

List of Tables

Chapter 1 Introduction

1.1 The impact of electric vehicles on air in megacities

Figure 1: Picture taken from Hong Kong Island in 2005 summer - mild air pollution period.

Figure 2: Picture taken from Hong Kong Island in 2005 winter - serious air pollution period.

Air pollution causes major problems in megacities like Hong Kong and Los Angeles. Many people, especially young children, suffer from some form of respiratory illnesses like asthma and bronchitis which has a huge impact on medical services and expenses.[1] World Health Organization (WHO) estimates suggest that air pollution causes approximately 2 million premature deaths worldwide per year.[2] Air pollution also has a significant effect on the domestic production forces and a strong impact on the tourist and commerce industries. It is incumbent on us to know how to reduce air pollution levels and make societies cleaner.

Particulate matters (PM_{10}, PM_{25}, and C_xH_y) and NO_x are the major pollutants and are caused mainly by large numbers of fossil-fuel driven vehicles. In order to reduce the amount of pollutants in megacities, one must decrease the use of fossil fuels, and one of the best ways to

do this is to reduce the number of vehicles. However, the implementation is not easily achieved because vehicles play an important and convenient role in our daily lives. A good alternative is to replace the fossil fuel-driven vehicles by zero-emission vehicle in cities, for example electric vehicles. Those are supported by many researches including the one from Argonne National Laboratory.[3] Their results show that the emission of particulate matters, NO_x, and other pollutants can be dramatically minimized in electric vehicles.[3] Higher fuel efficiency of electric vehicles is another advantage compared to fossil-fuel driven vehicles.[3] In order to support the mass production of electric vehicles, extensive research on rechargeable batteries must be conducted first so as to choose the best materials and optimize their performances.

Life cycle emission and fuel use per mile for gasoline and electric vehicle passenger cars

In urban	Gasoline-driven vehicles gram/mile	Electric vehicles gram/mile
Carbon monoxide (CO)	2.767	0.005
Volatile organic compounds (VOC)	0.148	0.000
Nitrogen oxides (NO_x)	0.048	0.015
PM10	0.032	0.022
Sulfur oxides (SO_x)	0.008	0.002

Figure 3: Dramatic reduction of air pollutants by replacing fossil fuel-driven vehicles by electric vehicles comparing to fossil fuel driven vehicles.[3]

1.2 Storage of renewable energies in rechargeable batteries

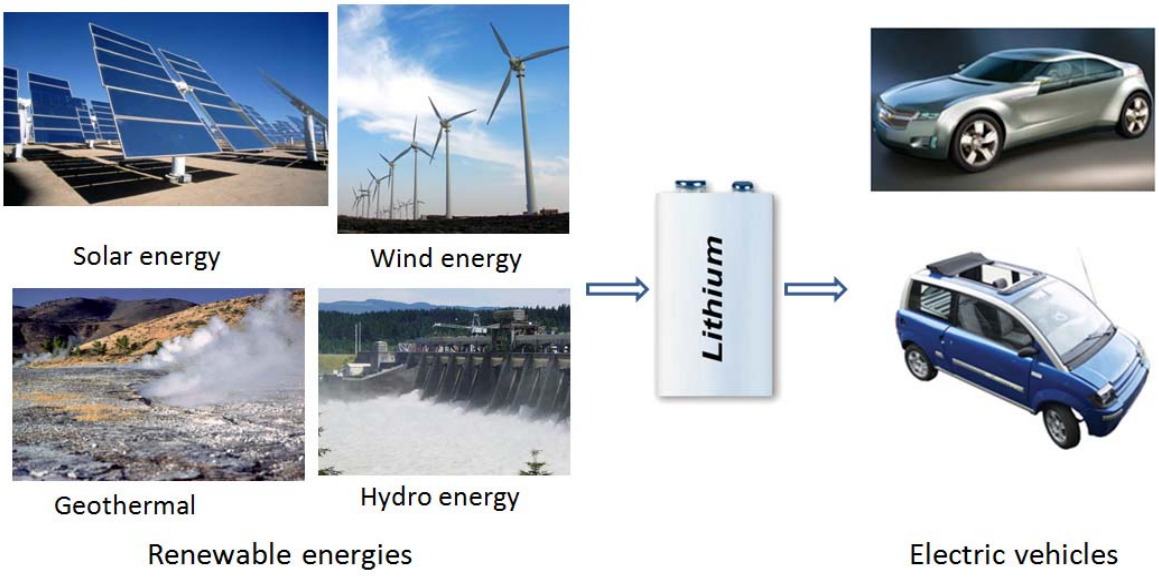

Figure 4: Renewable energies can be effectively stored in rechargeable batteries and utilized in portable electronic devices and electric vehicles.

Rechargeable batteries can be used to store different kinds of renewable energies such as solar energy, wind energy, geothermal energy, and hydro energy. Those energies are generated from natural resources and naturally replenished. With the good utilization of those renewable energies in our daily life, and reduction of our demand on fossil fuels, our energy cost can be highly reduced.

Moreover rechargeable batteries can also be utilized to solve load-leveling issue. The batteries are charged from electrical grid connected to electric power plants when the electric demand is low. The batteries supply electricity when the electric demand is high, which will reduce the demand for building new electric plants.

1.3 Advantages of lithium batteries as energy storage devices

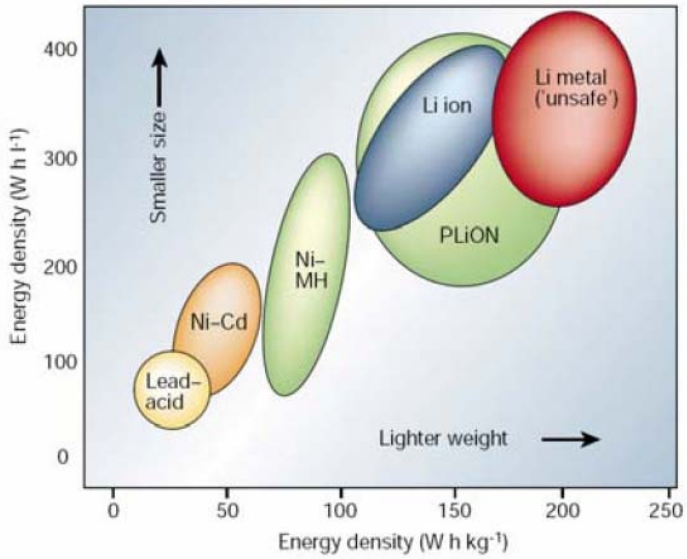

Figure 5: The energy density of lithium ion batteries is one of the highest battery systems comparing to other rechargeable battery systems.[4]

Development of batteries with high energy density is one of the most important concerns of battery companies. Energy density can be expanded by improving the packing efficiency of the active material in the battery, or by reducing the mass of the non-electrochemically active components, like carbon and binder. Since the active materials in lithium batteries have intrinsically high volumetric and gravimetric energy density, lithium batteries can already deliver reasonably large amounts of energy when compared with other rechargeable batteries on the market. This can explain why lithium batteries are expected to occupy 70% of the rechargeable battery market for portable electronic devices in Canada by 2010. [5] Furthermore, lithium batteries can be easily fabricated into various shapes, for instance, cylindrical, coin, prismatic, and ultra thin and flat, as shown in Figure 7. High flexibility

battery shape designs, together with intrinsically high energy density permit the cells to couple with the many portable electronic devices used in our daily life.

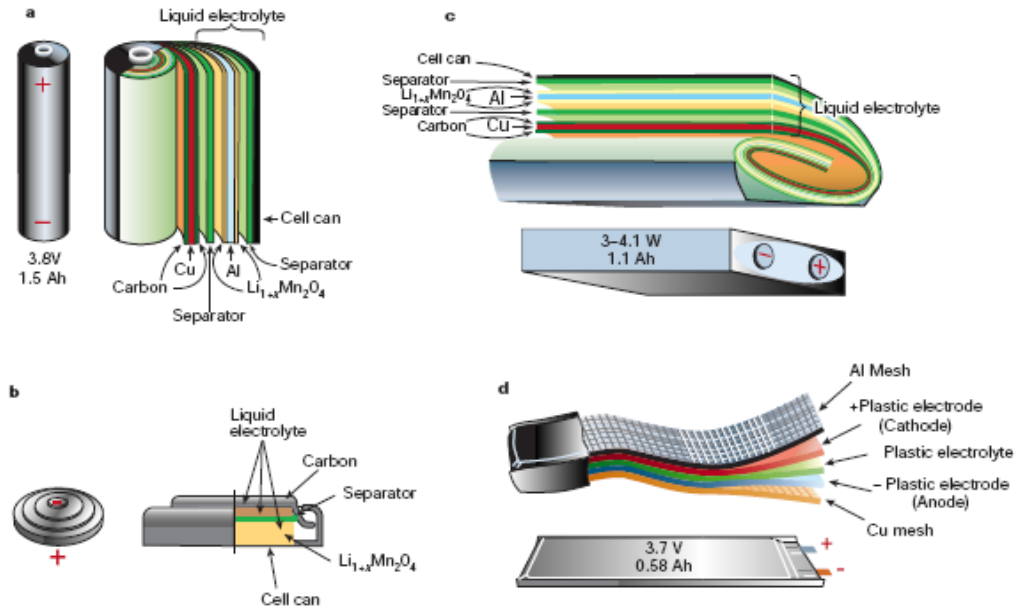

Figure 6: Lithium battery has very high design flexibility to be fabricated into different shapes: a. cylindrical, b. coin, c. prismatic, and d. thin and flat.[4]

Figure 7: Lithium batteries have many applications in various portable electronic devices: electric bikes, laptop computers, multi functional watches, and medical capsule camera.

1.4 Potential candidates for electric vehicles (EV) and hybrid electric vehicles (HEV)

Pb acid or NiCd batteries are utilized as power sources in conventional electric vehicles. However the practical range is quite short as the batteries have intrinsically low energy capacities as shown in Table 1 and Table 2. There are several other rechargeable batteries available that have higher energy capacities than Pb acid or NiCd batteries, for example NiMH or Li batteries. Lithium batteries have the highest energy capacity among the current rechargeable batteries, which allow automakers to design electric vehicles with reasonable long range. Moreover, a survey conducted by the department of transportation in the United States showed that 78 percent of Americans drive 40 mi (64.4 km) or less each day;[6] electric vehicles equipped with Li batteries can obviously meet the general demand of American drivers. In June 2008, GM first announced to produce noval electric vehicles called Chevy Volt and will launch to the market in 2010. The new Chevy Volt will be powered by lithium batteries manufactured by LG Chem and Compact Power Inc.

Technology	Pb Acid	NiCd	NiMH	Li-ion
Vehicle curb weight		1200 kg		
Battery weight allocation (typ.)		250 kg		
Battery structure cooling etc.		55 kg		
Module weight allocation		195 kg		
Energy density	33 Wh/kg	45 Wh/kg	70 Wh/kg	120 Wh/kg
Onboard energy	6.4 kWh	8.8 kWh	13.0 kWh	23.4 kWh
Calculated range @ 120Wh/ton/km	53 km	73 km	114 km	195 km

Table 1: Lithium battery has superior energy density comparing to other rechargeable battery systems for a typical size of 250 kg.[7]

Technology	Pb Acid	NiCd	NiMH	Li-ion
Battery volume allocation (typ.)			200 l	
Battery structure, cooling etc.			70 l	
Module volume allocation			130 l	
Volumetric Energy (module)	75 Wh/l	80 Wh/l	160 Wh/l	190 Wh/l
Onboard energy	9.8 kWh	10.4 kWh	20.8 kWh	24.7 kWh
Range @ 120 Wh/ton/km	81 km	87 km	173 km	206 km

Table 2: Lithium battery has very high volumetric density comparing to other rechargeable battery systems with a typical size of 200 l.[7]

The acceleration of an electric vehicle car is mainly determined by the battery power. In addition, the power also determines the time of the battery being charged. It is generally considered that a full-charge cycle should take about 6 hours at your house or office. Among the current rechargeable batteries, lithium batteries have the highest battery power as shown in Table 3.

Technology	Pb Acid	NiCd	NiMH	Li-ion
Vehicle curb weight			1200 kg	
Battery weight allocation (typ.)			250 kg	
Battery structure cooling etc.			55 kg	
Module weight allocation			195 kg	
Power density (module)	75 W/kg	120 W/kg	170 W/kg	370 W/kg
Battery Power	15 kW	24 kW	33 kW	72 kW

Table 3: Lithium battery has superior power performance comparing to other rechargeable systems with weight of 250 kg battery.[7]

Chapter 2 Research proposal

2.1 Reasons to choose $LiFePO_4$ cathode material as a candidate to study

Several promising lithium battery cathode materials, including spinel $LiMn_2O_4$, $LiCo_{1/3}Mn_{1/3}Ni_{1/3}O_2$, and $LiFePO_4$, have been extensively studied for more than 10 years.[1,2] They all have a reasonably high energy capacity (148 mAh/g in spinel $LiMn_2O_4$; 140 mAh/g in $LiCo_{1/3}Mn_{1/3}Ni_{1/3}O_2$; 170 mAh/g in $LiFePO_4$) suitable for high energy applications in, for example, electric vehicles. To ensure the safety, high energy batteries must be very stable under normal conditions and adverse environments such as high temperatures and overcharged conditions. Of the above candidates, $LiFePO_4$ is the most thermal and electrochemically stable material.[3] Considering that the rate performances of the materials are technically easy to improve, $LiFePO_4$ was chosen as a candidate to study on and improved its rate capability.

2.2 Research developments on $LiFePO_4$ in the last decade

Lithium iron phosphate, $LiFePO_4$, is a mineral that can be found in pegmatite granites, presented in other minerals such as phosphate, tourmaline and beryl.[4] In earlier studies, synthetic $LiFePO_4$ was mainly produced by solid state methods,[4] more recently, it is synthesized by utilizing various methods including hydrothermal synthesis,[5,6,7] sol-gel,[8,9,10] coprecipitation,[11,12] and polyol process,[13,14,15] for particle morphological controls and carbon coating purposes.

Conventional solid state synthesis:

Step 1: Preparation of precursor

$$Fe(OAc)_2 + (NH_4)_3PO_4 + 0.5\ Li_2CO_3 \xrightarrow[300\ ^oC - 350\ ^oC]{} \text{precursor}$$

Step 2: Crystallization of precursor

$$\text{precursor} \xrightarrow[800\ ^oC]{\text{Ar, 24 h}} LiFePO_4$$

Figure 8: The experimental procedures of the conventional solid state synthesis - one of the most popular synthetic methods for $LiFePO_4$.[17]

In early years, only a few researchers focused on the magnetic properties[4] and electron density analyses of $LiFePO_4$.[16] However, it has been a research focus since 1997 when Padhi and coworkers proposed it as an excellent candidate for the cathode of a low-power, rechargeable lithium battery that is inexpensive, nontoxic and environmentally benign.[17] The cell delivers a

relatively high capacity at an attractive working voltage (3.45V vs. Li^+/Li) at slow current rates as shown in Figure 9.

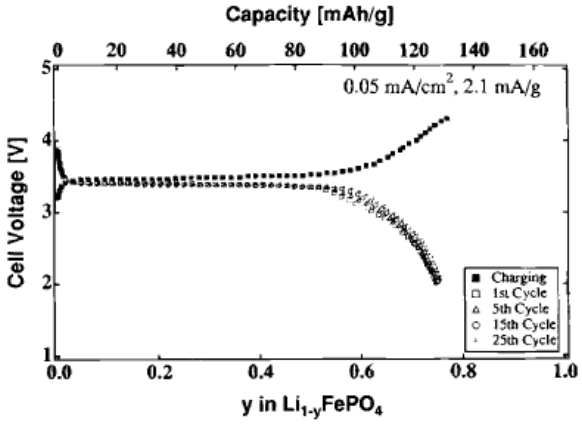

Figure 9: About 80% of the reversible capacity was obtained at C/85 current rate.[17]

More importantly, Padhi and coworkers demonstrated that the presence of polyanions (XO_4^{n-}, X = P or S) as these building blocks can raise the redox energy and can stabilize the structure from oxygen gas evolvement in high-temperature or over-charged conditions.[18] The presence of XO_4^{n-}, where X = P or S, as building blocks with strong X-O covalent bonds causes strong polarization of oxygen ions towards X, which reduces the covalence of Fe-O bonds and raises the redox energy through Fe-O-X inductive effect in $LiFePO_4$. Figure 10 shows the energy diagram of $Fe^{(n+1)+}/Fe^{n+}$ (n = 2, 3) redox couple in FeO_6 octahedra included in some iron-based cathode materials; the presence of phosphates or sulphates in the structure can raise the redox couple in FeO_6 octahedra by inductive effect.[19]

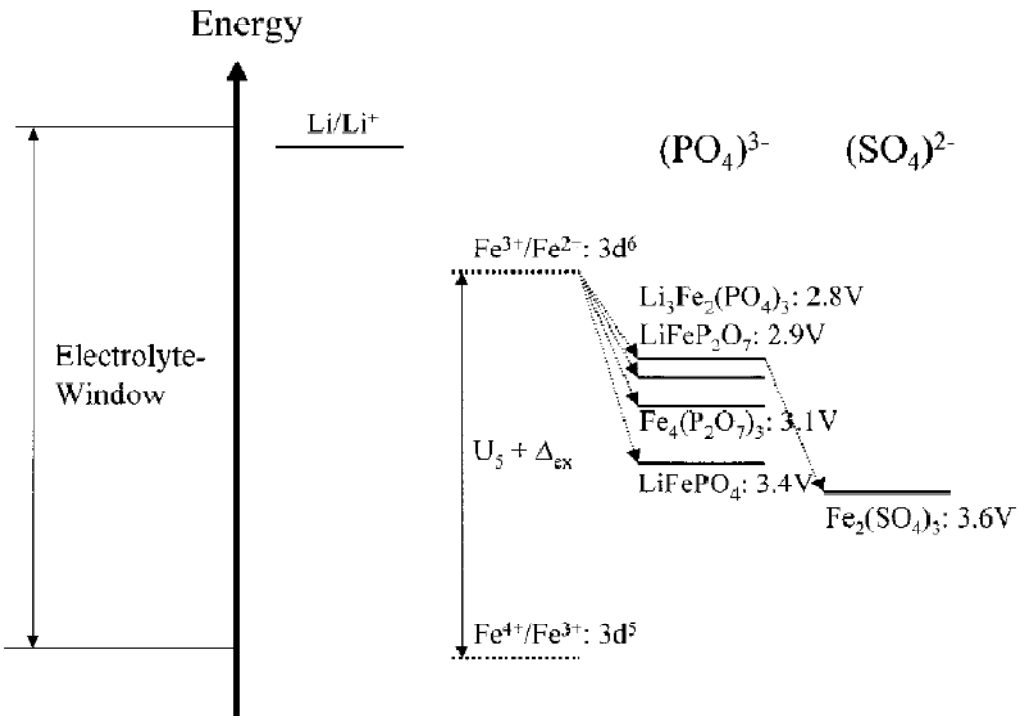

Figure 10: The schematic diagram shows $Fe^{(n+1)+}/Fe^{n+}$ (n = 2, 3) redox couple in FeO_6 octahedra can be raised when polyanions such as phosphates and sulphates are in the lattice.[19]

However, separation of the FeO_6 octahedra by phosphates reduces the electronic conductivity, limiting the electrons movement in two dimensions. Movement of lithium ions, on the other hand, is limited to one dimension along b-axis. It is supported by both theoretical calculations,[20,21] and experimental evidence.[22,23]

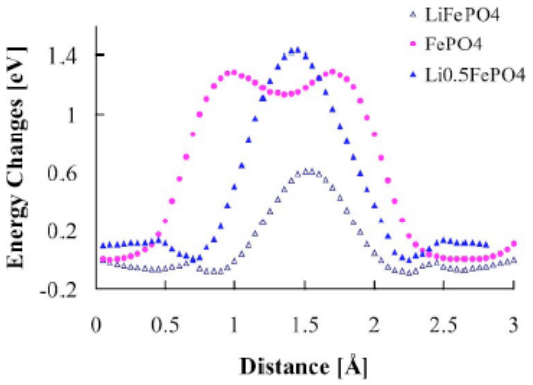

Figure 11: The activation energy for lithium ions to diffuse is the lowest along b axis (SG: *Pnma*) in $LiFePO_4$, $FePO_4$, and $Li_{0.5}FePO_4$, obtained from GGA calculations.[20]

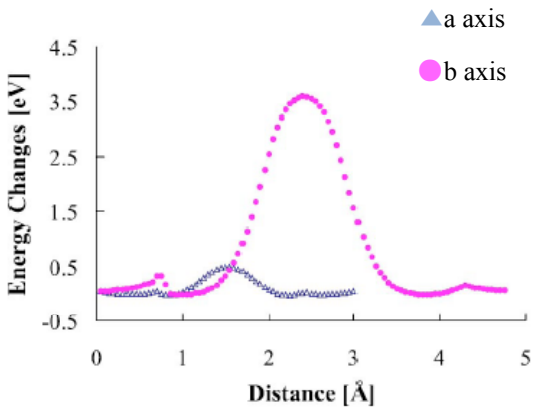

Figure 12: The activation energy for lithium ions to diffuse is the lowest along b axis in $LiFePO_4$ comparing to a axis (SG: *Pnma*), obtained from GGA calculations.[20]

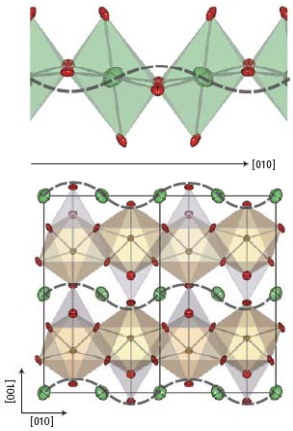

Figure 13: Lithium ions diffuse along b axis, followed by a curved pathway, observed from Rietveld refinement of neutron diffraction data.[22]

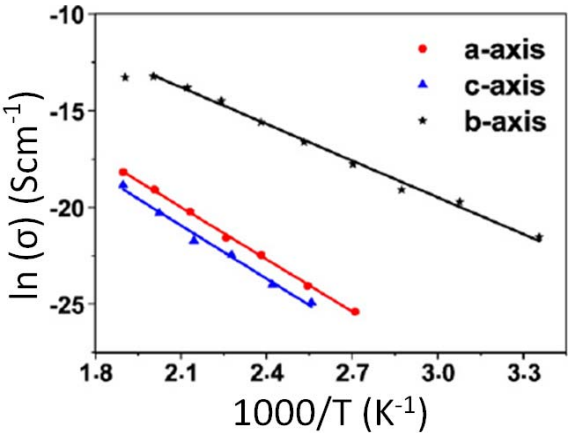

Figure 14: The ionic conductivity of lithium ions is the lowest along b axis comparing to a and c axes, from AC impedance spectroscopy in $LiFePO_4$ single crystals.[23]

However Maier and coworkers reported to observe the same ionic conductivity values along b and c axis (SG: *Pnma*), suggested that the chemical diffusivity of Li was two-dimensional (b-c

plane) in their single crystals.[24, 25] Those results shown in Table 4 were not expected in the view of the above computation predictions,[20,21] and the experimental evidences.[22,23]

Properties	a-axis	b-axis	c-axis
E_{eon}	0.59 eV	0.59 eV	0.55 eV
E_{ion}	0.74 eV	0.62 eV	0.62 eV
σ_{ion} at 300 K	1.5 X 10^{-14} Scm^{-1}	2.4 X 10^{-12} Scm^{-1}	2.9 X 10^{-12} Scm^{-1}
σ_{eon} at 300K	2.9 X 10^{-9} Scm^{-1}	5.6 X 10^{-8} Scm^{-1}	7.8 X 10^{-8} Scm^{-1}

Table 4: Both ionic and electronic conductivities of $LiFePO_4$ were observed to be 2-dimensional along b and c axes, by Maier and his coworkers.[24]

To explain the disagreement, Maier *et al.* further analyzed on the anti-site substitution of Li and Fe in the lattice position by single crystal X-ray diffraction and synchrontron X-ray radiation followed by Rietveld refinement analysis.[26] Their results showed that around 2.5% of iron occupied lithium positions. They explained this anti-site disorder blocked part of the Li ion diffusion channels along b-axes could lead to the observation of similar conductivity values along b and c axes. Lithium ions could need jump from one tunnel to another when the tunnels are blocked,[26]which could reduce the ionic conductivity along those directions (along b axis). Those anti-site disorders, on the other hand, can be dramatically reduced at higher preparation temperature.[27]

Additionally, Chen and coworkers reported that lithium ions' intercalation reactions occur only in nanometer interfaces between $FePO_4$ domains and $LiFePO_4$ domains in their 2 to 3 micron-sized crystallites from TEM measurements; simultaneously, intercalation reactions did not occur in every channel along b-axis.[28] The same phenomenon was also observed by Laffont

and coworkers by EELS measurements in their ca. 200 nm crystallites that lithium ions (de)intercalation reactions occurring in the nanometer interfaces.[29] Because of the intrinsically low electronic and ionic conductivities and the limitation of lithium ions (de)intercalation reactions occurring in the nanometer interface, high cell capacity could only be achieved at low current rates, which restricted the material from use in high-power applications.

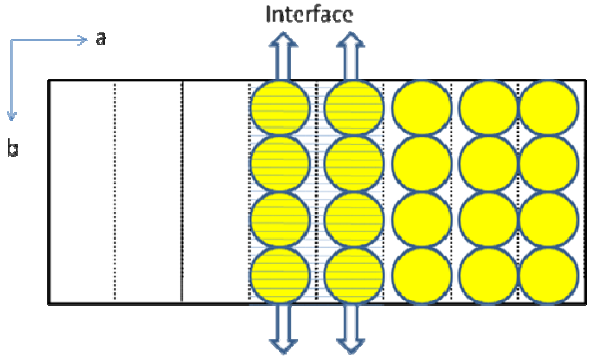

Figure 15: Lithium ions (de)intercalation reactions occur in nanometer interface in crystallites with sizes between 200 nm to 3 μm.

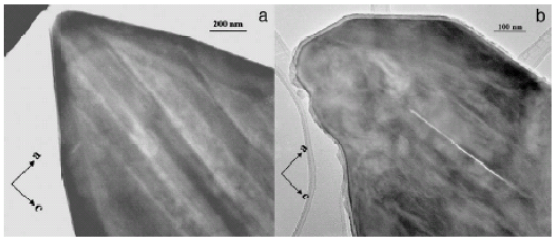

Figure 16: Order domains $FePO_4$ and $LiFePO_4$ were observed and well separated, from partially delithiated $Li_{0.5}FePO_4$ crystals, from TEM.[28]

Several techniques have been reported to improve the conductivities of $LiFePO_4$ in order to boost the electrochemical rate performances. Andersson and coworkers first reported significant improvement on the reversible capacity achieved by elevating the temperature.[30] Huang *et al.* and Armand *et al.* studied coating techniques on $LiFePO_4$ to enhance the electrochemical performances at room temperature.[31, 32] Huang obtained 90% theoretical capacity at C/2, with a very good rate capability and excellent stability, by a combination of conductive carbon and control of particle size to nanometer dimensions.[31] The presence of conductive carbon provided fast electronic transport between the current collector and the

individual particles; reducing particle size to nanometer dimensions offered shorter diffusion distances for lithium ions and electrons, which dramatically shortened the diffusion time ($t \sim l^2/d$; t: diffusion time, l: diffusion distances, d: diffusion coefficient) to promote good electrochemical performances at higher current rates.[33] More than 500 papers published have been focusing on the carbon coating techniques by various methods in the past decade.

It is now generally believed that $LiFePO_4$ could be one of the most promising cathode materials in lithium batteries as power sources for low power applications such as electric bicycles. However, it is more important to consider whether $LiFePO_4$ can be further improved for high-power applications, for example, electric and hybrid vehicles.

In principal, conductivities can be raised by increasing the number of charge-carriers in the material. For instance, in a $Li_\alpha MPO_4/Li_{1-\beta}MPO_4$ solid solution system, the addition of conductive additives, such as metallic powders or conductive carbon, can be minimized or eliminated thereby increasing the battery energy density.

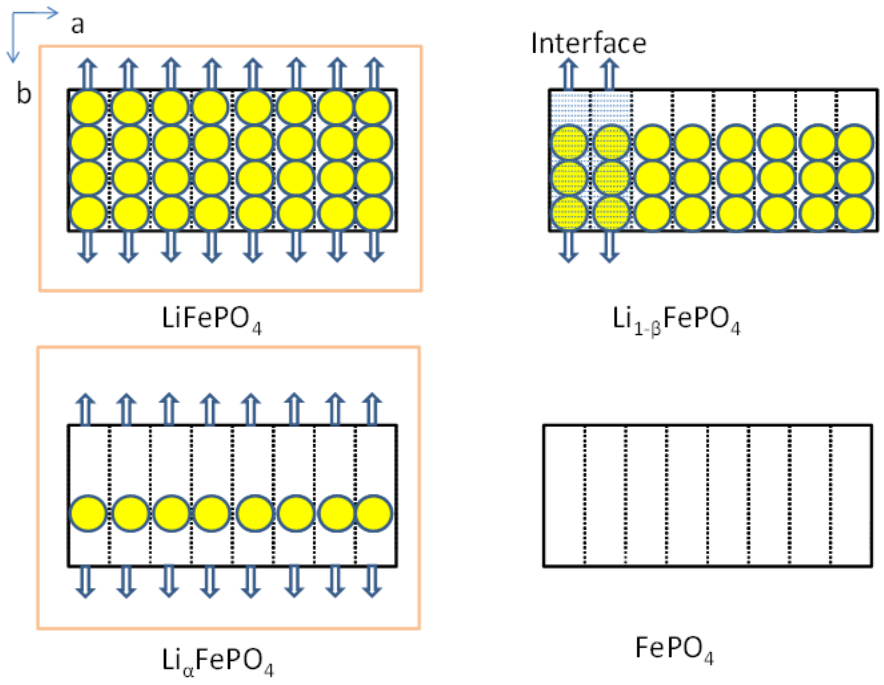

Figure 17: Charge carriers are more readily available in $Li_{\alpha}MPO_4/Li_{1-\beta}MPO_4$ solid solution system that promote faster lithium ions movement.

Chiang *et al.* attempted to synthesize $Li_{1-y}M_yFePO_4$ compounds by the doping method to sustain $Li_{\alpha}M_yFePO_4/Li_{1-\beta}M_yFePO_4$ solid solution systems; a small amount (around 1%) of supervalence cations ($M = Nb^{5+}$, Zr^{4+}, Ti^{4+}) was attempted to dope into the lattice in the lithium sites to sustain the substoichiometry cation deficient solid solution $Li_{1-y}M_yFePO_4$. They reported that electronic conductivity was boosted by a factor of 10^8 compared to the pure end member $LiFePO_4$.[34]

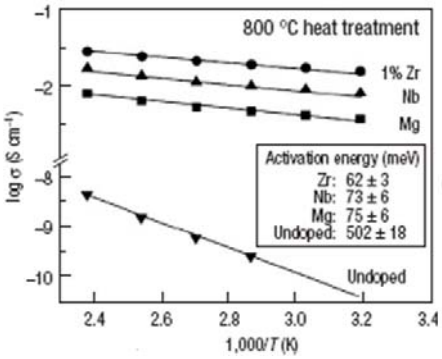

Figure 18: Dramaticaly electrical conductivity improvement was observed in doped samples comparing to undoped samples.[34]

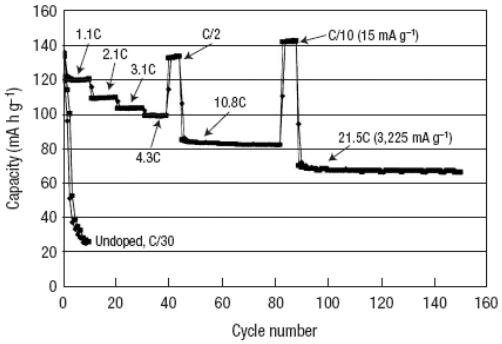

Figure 19: The rate performance was dramatically improved in doped samples comparing to undoped samples.[34]

Even though Chiang's exciting results of the impressive conductivity improvement supported the material being applied in the high power consumption applications, his explanation on the conductivity improvement was ambiguous. For instance, the doped $Li_{0.99}D_{0.01}FePO_4$ stoichiometry for supervalent cations such as Zr^{4+} implies a subvalent state of Fe on the basis of charge balance. Moreover, the detection limit of most of the powder X-ray diffractometers (XRD) is ca. 5 wt.%;[35] meaning that the measurement of 1% of dopant cannot be accurately addressed by XRD. Many arguments have been made on whether the contributing factor came from the doping effect or a purely carbon effect, due to the large amount of carbon content present in Chiang's samples.[36] Whether the amount of mixed valent Fe^{2+}/Fe^{3+} solid solution contributed to the capacity was not addressed carefully in the paper.

To address the above controversy, our group focused on the investigation of the role of conductive surface material (Fe_2P) generated in situ in high temperature reduced conditions by the carbothermal process. Subramanya *et al.* showed that a percolating nano-network of metal-

rich phosphides was responsible for the enhanced conductivity by promoting the electronic grain-boundary transport.[37] Similarly, conductivity improvement was also observed for non-doped samples. On the other hand, the presence of dopants within the lattice and their role in electrochemical improvement still had not been ascertained until a recent report by Wagemaker *et al.*[38] To address the problems, a series of doped samples were prepared those compositions were targeted to two categories: (1) $Li_{1-x}D_x^{y+}FePO_4$; (2) $Li_{1-yx}D_x^{y+}FePO_4$. Dopants concentrations and locations were characterized through the combination of neutron and X-ray diffraction studies. Their results showed that small amount of dopant (max. 3 mol%) located in the olivine lattice in their micron-sized samples. They were mainly presented on the Li-site. Since lithium ions diffuse in the channels along b-axis, the channels were partially blocked by the dopant. Moreover lithium vacancies, but not iron vacancies, were created to counterbalance the aliovalent charge of the dopant. Therefore the iron was still monovalent with charge +2; no additional charge carriers were created to improve the electronic conductivity.

Target stoichiometry	M1 and M2 composition [M1][M2]	Dopant M1/M2 occupancy ± 0.001	Fe M2 valence ± 0.006	Avg. M1-O distance (Å) ± 0.002
$LiFePO_4$	[Li][Fe]		2.000	2.150
	$Li_{1-x}D_xFePO_4$ compositions			
$Li_{0.99}Zr_{0.01}FePO_4$	$[Li_{0.979}Zr_{0.008}][Li_{0.008}Fe_{0.992}]$	0.008/0.000	1.998	2.151
$Li_{0.96}Zr_{0.04}FePO_4$	$[Li_{0.966}Zr_{0.009}][Li_{0.007}Fe_{0.993}]$	0.009/0.000	2.003	2.153
$Li_{0.99}Nb_{0.01}FePO_4$	$[Li_{0.986}Nb_{0.005}][Li_{0.007}Fe_{0.993}]$	0.005/0.000	1.998	2.152
	$Li_{1-xy}D_x^{y-}FePO_4$ compositions			
$Li_{0.96}Zr_{0.01}FePO_4$	$[Li_{0.976}Zr_{0.008}][Li_{0.004}Fe_{0.996}]$	0.008/0.000	1.996	2.154
$Li_{0.88}Zr_{0.03}FePO_4$	$[Li_{0.891}Zr_{0.022}][Li_{0.004}Zr_{0.009}Fe_{0.987}]$	0.023/0.008	2.005	2.157
$Li_{0.91}Cr_{0.03}FePO_4$	$[Li_{0.924}Cr_{0.021}][Cr_{0.008}Fe_{0.992}]$	0.021/0.008	2.004	2.156

Table 5: The presence of dopants in the lattices and the valant state of Fe in doped samples were studied by both X-ray and neutron diffractions, by Wagemarker and his coworkers.[38]

Even through the presence of Fe^{2+}/Fe^{3+} solid solution system was shown to be absent in the doped samples by Wagemarker and coworkers,[38] researchers were still interested in locating the Fe^{2+}/Fe^{3+} solid solution system and addressing its contributions to electronic and ionic conductivities in the mixed valent environment. The temperature-driven Fe^{2+}/Fe^{3+} solid solution property in Li_xFePO_4 for $0 \leq x \leq 1$ was first observed by Delacourt and coworkers;[39] single solid solution phase Li_xFePO_4 was formed from two-phase $LiFePO_4/FePO_4$ system at elevated temperatures. The driving force was due to the increase of the entropy contribution to the Gibbs free energy at high temperatures; lithium ions were thermodynamically stable under disordered arrangement in the lattice.

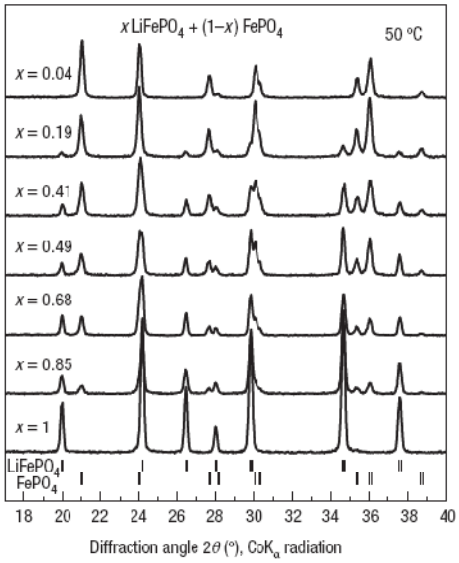

Figure 20: Two-phase mixture $LiFePO_4$/ $FePO_4$ was observed in low temperature condition, from XRD.

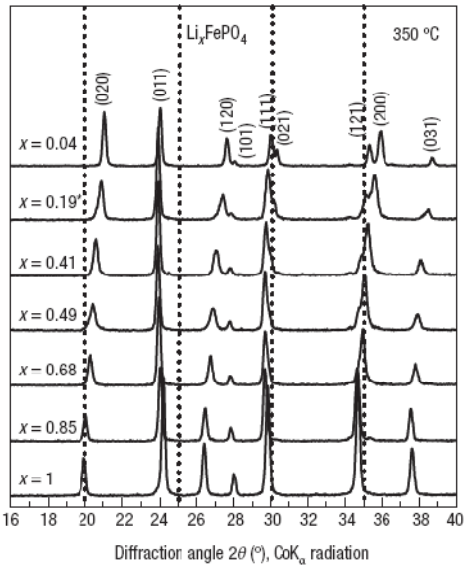

Figure 21: Single solid solution phase Li_xFePO_4 was observed at elevated temperature.

Ellis and coworkers further investigated the onset temperature of electron delocalization and its correlation to the state of lithium disorder.[40] They have shown that electron delocalization in the solid solution phase formed at elevated temperature was due to rapid small polaron hopping (with hopping frequency 10^8 sec^{-1}). Their Mössbauer measurements pinpointed the temperature of formation of solid solution on heating $LiFePO_4/FePO_4$ above 500 K, the electron and lithium delocalization events were strongly correlated suggested that they were coupled.

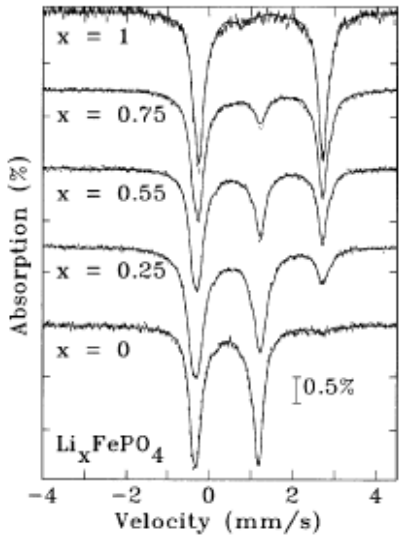

Figure 22: Monovalent Fe^{2+} and Fe^{3+} ions were observed in $LiFePO_4$ and $FePO_4$ respectively; monovalent Fe^{2+} and Fe^{3+} ions were observed in $Li_{0.85}FePO_4$, $Li_{0.55}FePO_4$ and $Li_{0.25}FePO_4$ at room-temperature, from Mössbauer measurements.

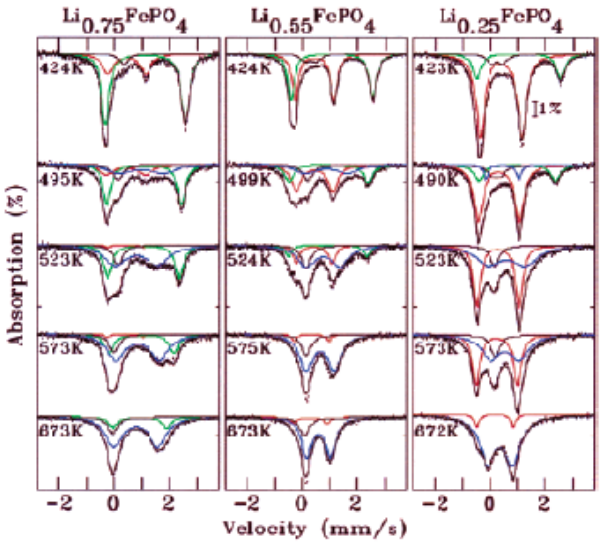

Figure 23: Mixed-valent ions were observed in $Li_{0.75}FePO_4$, $Li_{0.55}FePO_4$ and $Li_{0.25}FePO_4$ at elevated temperatures, from Mössbauer measurements.

Yamada and coworkers later reported that the formation of partially solid solution $Li_{\alpha}FePO_4$ and $Li_{1-\beta}FePO_4$ end members was size dependent; some amount of disorder corresponding for $\alpha = 0.05$ and $1-\beta = 0.89$ was observed at room temperature for particles with size ca. 100 nm by the neutron diffraction technique.[41] The results suggest a smaller miscibility gap will be observed when crystalline sizes are smaller; and a full solid solution system could be observed when crystalline sizes continue below a threshold value.

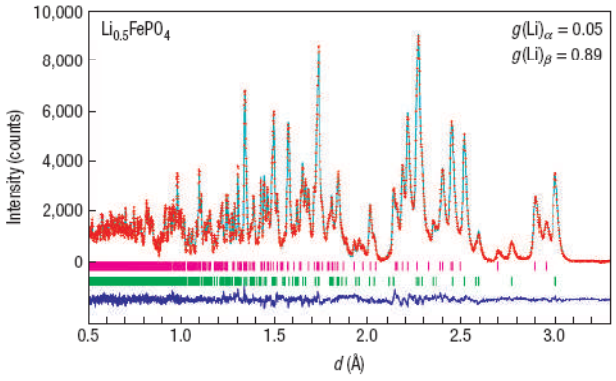

Figure 24: Mixed-valent ions were observed in end members in partially delithiated samples at room temperature, from Rietveld refinements.[41]

The reduction of miscibility gaps for particles below 100 nm was further confirmed by Chiang and coworkers for various sizes of particles at different temperatures shown in Figure 25 and Figure 26.[42] They have anticipated that full solid solution single phase Li_xFePO_4 could be observed when crystalline sizes are below about 15 nm at 25°C or about 25 nm at 45°C. [42] Nonetheless, typical two-phase reaction $LiFePO_4/FePO_4$ (or $Li_{1-\alpha}FePO_4/Li_\beta FePO_4$ precisely) was still observed from the electrochemical measurements of 20 X 50 nm $LiFePO_4$ nanocrystallites prepared by polyol process shown in Figure 27 and Figure 28.[13] Due to the lack of synthetic routes to prepare nanocrystallites with sizes below 15 nm, it is still unclear whether the two end members $Li_{1-\alpha}FePO_4/Li_\beta FePO_4$ can be completely miscible under certain size regime at ambient conditions.

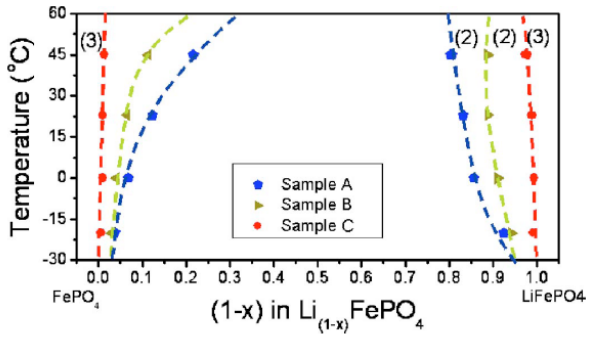

Figure 25: The miscibility gap was observed to be reduced when particle size reduced or temperature increased.[42]

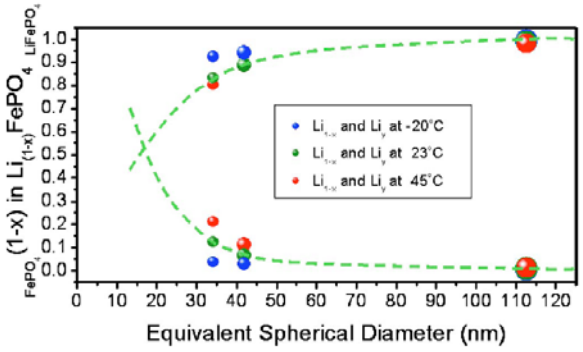

Figure 26: The amount of solid solution in end members was highly dependent on particle size and temperature.[42]

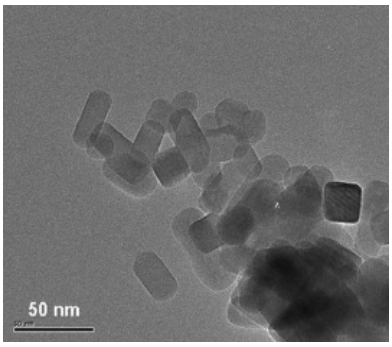

Figure 27: $LiFePO_4$ particles with size 20 X 50 nm were observed in TEM, prepared from polyol process.[13]

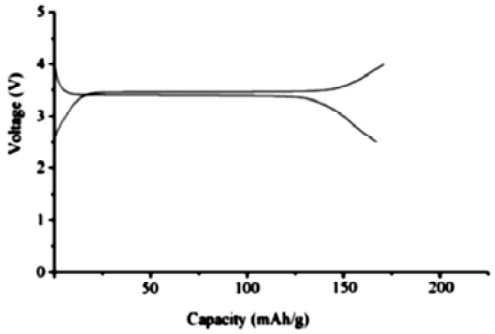

Figure 28: The voltage profile of $LiFePO_4$ samples prepared in polyol process at current density of 0.1 mA/cm^2.[13]

More recently Masquelier *et al.* reported to fabricate 40 nm lithium iron phosphate crystallites which shown room temperature single-phase Li insertion/extraction behaviour.[43] Those lithium iron phosphate samples were synthesized by the precipitation route in aqueous solution at low temperature and hence contained a lot of antisite defects and cation vacancies. The present of those defects and vacancies would reduce the capacity of the amount of charges being stored. Nonetheless they played an important role to minimize the volume change between two end members, which could improve the kinetic for phase transformation. Even through the fact that lithium (de)intercalation reaction can be occurred through all of the channels along b axis (SG:

Pnma) simultaneously, their electrochemical behaviours were quite unsatisfactory; reversible capacity of 70% was obtained at C/10 current rate. The poor electrochemical performance was partially due to the fact that some amount of Fe (ca. 6%) in Li-site which blocked the channels for lithium ions from (de)intercalation. Moreover long inter-particular diffusion lengths for electrons in these non-carbon coated samples limited the materials rate performances.

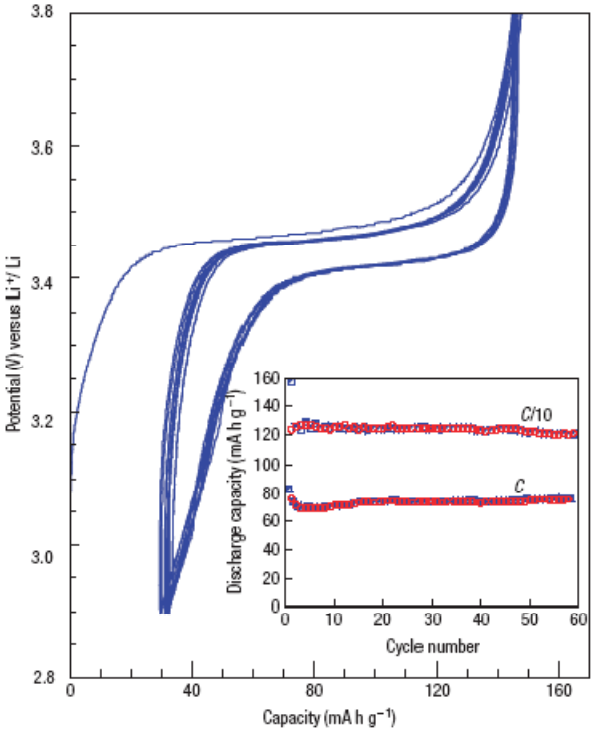

Figure 29: The voltage profile of non-carbon coated samples at C/10 current rate.[43]

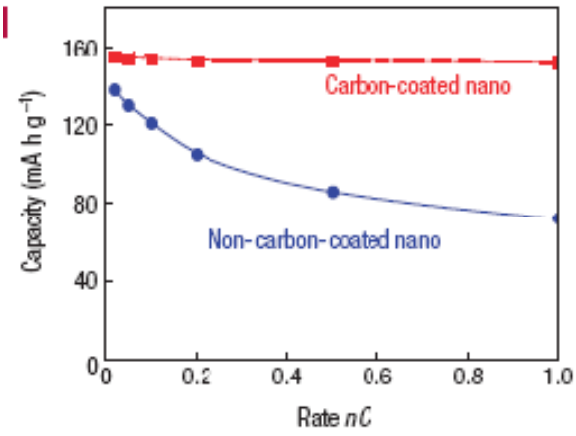

Figure 30：Carbon coated and non-carbon coated samples showed different rate performances.[43]

To conclude, carbon coated $LiFePO_4$ defect-free nanocrystallites are expected to have specific solid solution behaviour to be beneficial to the battery rate performance because of the larger number of charge carriers in the mixed Fe^{2+}/Fe^{3+} systems in the two end members. In addition, those nanocrystallites are more accessible to the electrolyte than micro-sized crystallites; lithium ions can be intercalated readily in the former samples. Moreover those nanocrystallites

offer short diffusion distances for lithium ions and electrons, which shorten the diffusion time. However non-carbon coated defective nanocrystallies have been shown to have poor electrochemical performances due to anti-site disorder and long diffusion length for electrons.

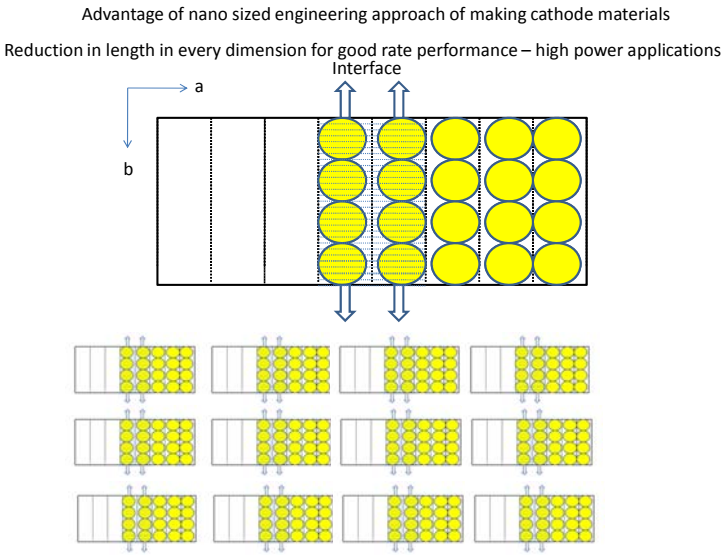

Figure 31: Nanocrystallites are more accessible to the electrolyte comparing with bulk crystallites; lithium ions can be easily (de)intercalated in the lattice more readily.

Very recently, Laffont and coworkers observed a new lithium ions intercalation phenomenon for $LiFePO_4$ nanocrystallites with sizes ca. 100 nm; the growth reaction of the new phase could be faster than its nucleation. Comparing with micron-sized and nano-sized crystallites, nanocrystallites have fewer the number of $[FeO_4]_n$ planes involved in the boundary to accommodate the different in structures between two end members during the (de)intercalation reaction. Such small local constraints could be stable in the structure to drive fast boundary displacement. The coexistence of fully intercalated and fully deintercalated individual particles were observed in the electrochemically partially deintercalated nanocrystalline samples by X-ray diffractometry and electron microscopy.[44] Laffont named the new phenomenon a domino-cascade model.

Estimated formular		FWHM (deg.)			a (Å)	b (Å)	c (Å)	<L> (Å)
	$Li_{1-\beta}FePO_4$	(200)	(210)	(311)				
	$Li_{\alpha}FePO_4$	(200)	(210)	(020)				
$LiFePO_4$		0.07	0.08	0.09	10.3294	6.0086	4.6948	740 ± 20
'$Li_{\sim 0.96}FePO_4$'	$Li_{1-\beta}FePO_4$	0.06	0.08	0.09	10.3235	6.0044	4.6925	750 ± 60
	$Li_{\alpha}FePO_4$	0.07	0.09	-	9.84	5.8	4.79	-
'$Li_{\sim 0.83}FePO_4$'	$Li_{1-\beta}FePO_4$	0.05	0.07	0.08	10.3238	6.0049	4.693	800 ± 30
	$Li_{\alpha}FePO_4$	0.10	0.10	0.13	9.827	5.7961	4.7834	730 ± 20
'$Li_{\sim 0.72}FePO_4$'	$Li_{1-\beta}FePO_4$	0.06	0.06	0.08	10.3238	6.005	4.6937	700 ± 20
	$Li_{\alpha}FePO_4$	0.10	0.12	0.12	9.826	5.7956	4.7814	600 ± 50
'$Li_{\sim 0.61}FePO_4$'	$Li_{1-\beta}FePO_4$	0.07	0.07	0.08	10.3222	6.004	4.693	730 ± 40
	$Li_{\alpha}FePO_4$	0.10	0.12	0.13	9.826	5.7956	4.7811	650 ± 70
'$Li_{\sim 0.53}FePO_4$'	$Li_{1-\beta}FePO_4$	0.07	0.07	0.09	10.3224	6.0043	4.6932	700 ± 20
	$Li_{\alpha}FePO_4$	0.10	0.12	0.14	9.828	5.7955	4.7811	750 ± 60
'$Li_{\sim 0.39}FePO_4$'	$Li_{1-\beta}FePO_4$	0.08	0.06	0.08	10.323	6.0041	4.6939	820 ± 100
	$Li_{\alpha}FePO_4$	0.09	0.11	0.14	9.828	5.7958	4.7817	930 ± 140
'$Li_{\sim 0.36}FePO_4$'	$Li_{1-\beta}FePO_4$	0.10	0.08	0.10	10.322	6.0039	4.694	650 ± 70
	$Li_{\alpha}FePO_4$	0.10	0.11	0.13	9.827	5.7955	4.7805	700 + 60
'$Li_{\sim \alpha}FePO_4$'	$Li_{1-\beta}FePO_4$	-	-	-				-
	$Li_{\alpha}FePO_4$	0.07	0.09	0.11	9.8207	5.7913	4.7798	760 ± 100

Table 6: Diffraction peaks with similar FWHM values were observed from end members of a two-phase mixture in Li_xFePO_4 samples under different stages of charges.[44]

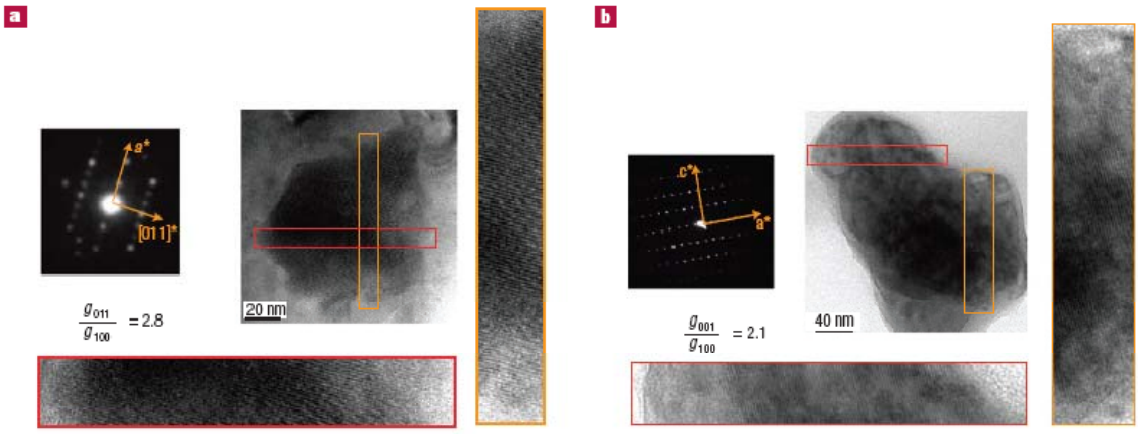

Figure 32: Single ordered domains were observed in partially delithiated particles, from high-resolution TEM images.[44]

2.3 Research objectives

1) Advantages of nanocrystallites were introduced to be beneficial for electrochemical performance. However, since their solid solution behaviours are not yet well understood, further studies will be conducted to understand the factors that can sustain a stable full solid solution phase in ambient conditions. As we know that the formation of solid solution phases is size and temperature dependent, suitable sizes of crystallites must first be prepared for solid solution behaviour studies. As such, our first target is to synthesize $LiFePO_4$ crystallites with various sizes, from 5 nm to 200 nm, which will be made by two solution methods: hydrothermal synthesis and polyol process. These are two of the principal synthetic methods for preparing new inorganic materials.

   Various sizes and shapes of nanomaterials, for example, oxides,[45] phosphates,[46] and silicates,[47] which are functional in catalysis,[48,49] electrochemistry,[50] and separation science,[51] have been produced in hydrothermal synthesis. Control of the sizes and shapes of nanomaterials come from the manipulation of experimental parameters, including precursors concentration,[52] reaction temperature,[53] solvent system,[54] experimental time,[55] and pH.[56]

   For decades, polyol process has been one of the most common soft chemistry methods for the preparation of micron and submicron particles.[57,58,59] In the past, the process was mainly applied in making micron-sized metals for catalytical purposes.[60] Later on it

was further explored in making other binary and tertiary complex compounds, such as nanospheres,[61] nanocubic,[62] and nanorod,[61] to study their specific properties.

The synthetic procedures involve the use of polyol, alcohols containing more than one hydroxyl groups, as solvent, and a reducing agent; pure samples can be synthesized in polyol solution under boiling conditions for various lengths of time. Samples prepared in polyol process usually converted with a thin polymer layer (around 1 – 2 nm) formed when some of the polyol solution is decomposed under high temperature. Even though the thin layer is a minor impurity phase present in the samples, it is very important to prevent the crystallites from becoming bigger in size; in other words, it is an effective size stabilizer in the polyol process.

2) Various sizes of $LiFePO_4$ crystallites will be studied for their solid solution behaviour at ambient conditions and elevated temperatures. It has been suggested by Chiang and coworkers that complete solid solution system could be formed at room temperature for crystallites with a size below about 15 nm at ambient conditions or below about 25 nm at 45^{o}C.[42] However, experimental evidence has not been reported due to the difficulty in making nanocrystallites in various sizes. We are interested to see if Li_xFePO_4 full solid solution systems can be formed in ambient conditions and to address their properties, including thermal stability, electrochemical stability, and air and moisture sensitivities, something important to know before mass producing the materials for use in high power applications.

3) Various sizes of $LiFePO_4$ nanocyrstallites will be used to examine the temperature-driven solid solution property of Li_xFePO_4 ($x \in [0, 1]$) to see whether nanocrystallites could have impacted on the transition temperature. It will be interesting to see if lowering transition temperature or ambient conditions are enough to drive the formation of the solid solution phase, which could have a strong influence on the optimal temperature and crystalline size for electrochemical performances.

4) The same synthetic techniques and methodologies will be applied to other olivine members with higher working voltages, for instance $LiMnPO_4$, $LiCoPO_4$, and $LiNiPO_4$, to see whether they too can be extended to other systems. These olivine members have very low electronic and ionic conductivities. If their conductivities can be improved by creating more charge carriers in the system, for example in nanocrystalline materials at room temperature or elevated temperature conditions, these materials will be very suitable for both high energy and power applications.

Chapter 3 Experimentals

3.1 Hydrothermal synthesis

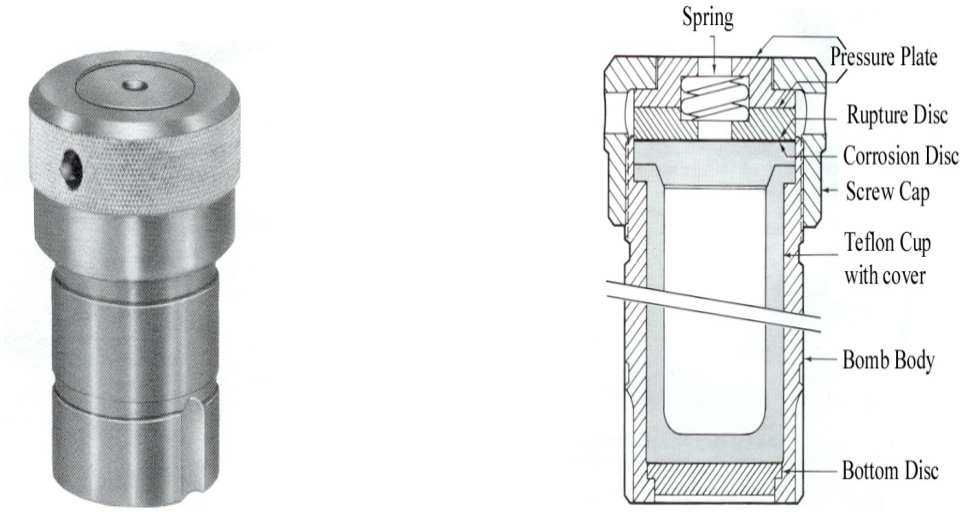

Figure 33: Hydrothermal reaction setup for the synthesis of $LiFePO_4$ nanocrystallies.

3.1.1 Synthesis of 200 nm $LiFePO_4$ tablet nanocrystallites

$NH_4FePO_4 \cdot H_2O$ was prepared by mixing ascorbic acid, $FeSO_4 \cdot 7H_2O$ (98% - Aldrich), H_3PO_4 (85 wt.% in H_2O - Fisher) and $NH_3 \cdot H_2O$ (28 - 30 wt.% in H_2O - EMD^{TM}) in a 0.1:1:1:3 molar ratio. The solid residue was filtered off and washed with water and acetone; then dried in a vacuum oven at 60^oC for 3 hours. 200 nm $LiFePO_4$ tablet nanocrystallites were prepared by mixing $NH_4FePO_4 \cdot H_2O$, $LiOH \cdot 2H_2O$ (98% - Aldrich) and ascorbic acid (99% - Aldrich) in a 4:4:3 molar ratio, typically using a concentration of $NH_4FePO_4 \cdot H_2O$ of 0.133 M. The reagents

were placed in an autoclave which was heated at 190°C for 15 hours. The product was filtered off and dried in a vacuum oven at 60°C for 3 hours.

3.1.2 Synthesis of 50 nm $LiFePO_4$ nanocrystallites

$NH_4FePO_4 \cdot H_2O$ was prepared by mixing ascorbic acid, $FeSO_4 \cdot 7H_2O$ (98% - Aldrich), H_3PO_4 (85 wt.% in H_2O - Fisher) and $NH_3 \cdot H_2O$ (28 - 30 wt.% in H_2O - EMD™) in a 0.1:1:1:3 molar ratio. The solid residue was filtered off and washed with water and acetone; then dried in a vacuum oven at 60°C for 3 hours. 50 nm $LiFePO_4$ tablet nanocrystallites were prepared by mixing $NH_4FePO_4 \cdot H_2O$, $LiOH \cdot 2H_2O$ (98% - Aldrich) and ascorbic acid (99% - Aldrich) in a 4:4:3 molar ratio, typically using a concentration of $NH_4FePO_4 \cdot H_2O$ of 0.4M. The reagents were placed in an autoclave which was heated at 190°C for 15 hours. The product was filtered off and dried in a vacuum oven at 60°C for 3 hours.

3.2 Polyol Process

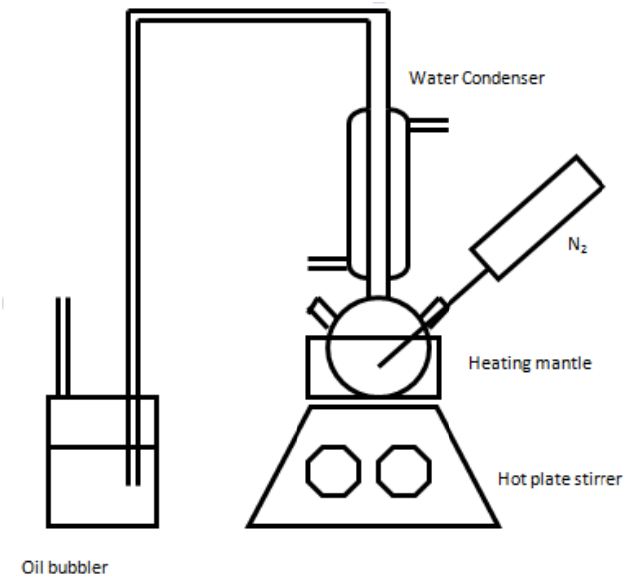

Figure 34: Polyol reaction setup for the synthesis of $LiFePO_4$ nanocrystallites.

3.2.1 Synthesis of 25 X 100 nm $LiFePO_4$ nanorods

$$LiOAc + Fe(OAc)_2 + NH_4H_2PO_4 \xrightarrow[\text{reflux}]{\text{320°C, Tetraethylene glycol}} LiFePO_4$$

25 X 100 nm $LiFePO_4$ nanorods were prepared by mixing LiOAc (99.99% - Aldrich), $Fe(OAc)_2$ (99.99% - Aldrich) and $NH_4H_2PO_4$ (97% - Aldrich) in a 1:1:1 molar ratio, typically using a concentration of LiOAc of 0.0625 M in tetraethylene glycol (99% - Aldrich). The reagents were placed in a round bottom flask which was connected to a reflux condenser. The solution mixture was stirred and maintained at 320°C for 20 hours under a nitrogen atmosphere.

The product was centrifuged and washed several times with acetone to remove the tetraethylene glycol. Samples were dried in a vacuum oven at 160^{o}C for 1 day.

3.2.2 Synthesis of 15 X 50 nm $LiFePO_4$ nanoneedles

15 X 50 nm $LiFePO_4$ nanoneedles were prepared by mixing LiOAc (99.99% - Aldrich), $Fe(OAc)_2$ (99.99% - Aldrich) and $NH_4H_2PO_4$ (97% - Aldrich) in a 1:1:1 molar ratio, typically using a concentration of LiOAc of 0.0625 M in tetraethylene glycol (99% - Aldrich). The reagents were placed in a round bottom flask which was connected to a reflux condenser. The solution mixture was stirred and maintained at 320^{o}C for 3 hours under a nitrogen atmosphere. The product was centrifuged and washed several times with acetone to remove the tetraethylene glycol. Samples were dried in a vacuum oven at 160^{o}C for 1 day.

3.2.3 Synthesis of 50 X 100 nm $LiMnPO_4$ nanocrystallites

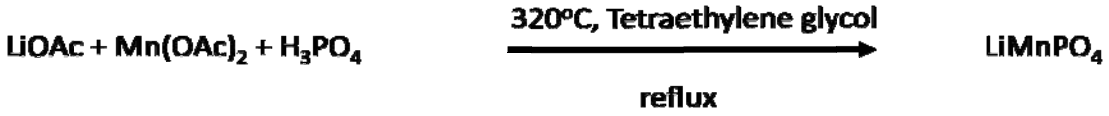

50 X 100 nm $LiMnPO_4$ nanorods were prepared by mixing $LiOAc{\cdot}2H_2O$ (98% - Aldrich), $Mn(OAc)_2{\cdot}4H_2O$ (98% - Alfa Aesar) and H_3PO_4 (85 wt.% in H_2O- Fisher) in a 1:1:1 molar ratio, typically using a concentration of LiOAc of 0.0625 M in tetraethylene glycol (99% - Aldrich). The reagents were placed in a round bottom flask which was connected to a reflux condenser. The solution mixture was stirred and maintained at 320°C for 20 hours under a nitrogen atmosphere. The product was centrifuged and washed several times with acetone to remove the tetraethylene glycol. Samples were dried in a vacuum oven at 160°C for 1 day.

3.2.4 Synthesis of 30 X 50 nm $LiMnPO_4$ nanocrystallites

30 X 50 nm $LiMnPO_4$ nanorods were prepared by mixing $LiOAc{\cdot}2H_2O$ (98% - Aldrich), $Mn(OAc)_2{\cdot}4H_2O$ (98% - Alfa Aesar) and H_3PO_4 (85 wt.% in H_2O - Fisher) in a 1:1:1 molar ratio, typically using a concentration of LiOAc of 0.0625 M in tetraethylene glycol (99% - Aldrich). The reagents were placed in a round bottom flask which was connected to a reflux condenser. The solution mixture was stirred and maintained at 320°C for 3 hours under a nitrogen atmosphere. The product was centrifuged and washed several times with acetone to remove the tetraethylene glycol. Samples were dried in a vacuum oven at 160°C for 1 day.

3.2.5 Synthesis of 50 X 200 nm $LiCoPO_4$ nanocrystallites

50 X 200 nm $LiCoPO_4$ nanorods were prepared by mixing LiOAc (99.99% - Aldrich), $Co(OAc)_2 \cdot 4H_2O$ (98% - Alfa Aesar) and H_3PO_4 (85 wt.% in H_2O - Fisher) in a 1:1:1 molar ratio, typically using a concentration of LiOAc of 0.0625 M in tetraethylene glycol (99% - Aldrich). The reagents were placed in a round bottom flask which was connected to a reflux condenser. The solution mixture was stirred and maintained at 320^oC for 20 hours under a nitrogen atmosphere. The product was centrifuged and washed several times with acetone to remove the tetraethylene glycol. The product was then heated in a tube furnace at a temperature of 650^oC or higher under an Argon atmosphere for 0.5 hour or longer.

3.2.6 Preparation of 25 X150 nm $Li_{0.5}FePO_4$ nanorods

25 X 150 nm $Li_{0.5}FePO_4$ nanorods were prepared by mixing the as-prepared $LiFePO_4$ and $NOBF_4$ (95% - Aldrich) in a 2:1 molar ratio in acetonitrile (99.8% - Aldrich). The reaction was carried in an argon atmosphere for 1 hour. The product was filtered off and was washed with acetonitrile. It was then dried in a vacuum oven at 60^{o}C for 3 hours.

3.2.7 Preparation of 50 X 100 nm $Li_{0.5}MnPO_4$ nanocryatallites

50 X 100 nm $Li_{0.5}MnPO_4$ nanocrystallites were prepared by mixing the as-prepared $LiMnPO_4$ and NO_2BF_4 (95% - Aldrich) in a 2:1 molar ratio in acetonitrile (99.8% - Aldrich). The reaction was carried in an argon atmosphere for 5 days or longer. The product was filtered off and was washed with acetonitrile. It was then dried in a vacuum oven at 60^{o}C for 3 hours.

Chapter 4 Characterization methods

4.1 Powder X-ray diffraction (XRD)

X-ray powder diffraction was performed on a Bruker D8-Advantage powder diffractometer equipped with a graphite monochromator and a nickel filter, operating at 40 kV and 30 mA, using Cu-Kα radiation (λ = 1.54 Å). Wide angle measurements were performed with 3 slits, two with a 2.0 mm width and one with 0.6 mm width, to control the beam size. Powder samples were mounted in aluminum sample holders in a flat geometry. The conventional scan rate was 0.05^{o} per second from $2\theta = 10^{o}$ to 80^{o}, while the high resolution scan rate was 0.02^{o} per 8 seconds from $2\theta = 10^{o}$ to 80^{o} for refinement purposes. The Rietveld method, GSAS with EXOGUI interface, was used to refine the datasets. Background, zero, scale factor, lattice parameters, atom positions, Uiso values and coefficients for the peak shape and size functions were refined until convergence was achieved.

Coherence length analyses of nanocrystallites for sizes equal to or below 100 nm were performed using the Scherrer equation based on the broadening diffraction effect:

$$d = \frac{0.9\lambda}{\beta_{1/2}\cos\theta}$$

where λ is X-ray radiation wavelength, $\beta_{1/2}$ is the full width half maximum of the diffraction peak in radians, θ is the Bragg angle which construction interference occurred.

4.2 Variable temperature X-ray diffraction (VT-XRD)

Variable temperature X-ray diffraction was performed in an INEL powder diffractometer with a position-sensitive detector operating at 30 kV and 30 mA using Cu$K\alpha_1$ radiation equipped with CPS 120 - CM detector. Samples were mounted in ceramic sample holders in a flat geometry, which were put into an air-tight furnace under the flow of He gas at around 0.5 cm^3/second. The furnace temperature was raised at 10^oC/minute and the temperature was maintained for 2 hours. The XRD patterns were measured after the temperature had been stabilized at certain values for 1 hour. Since the scan angle and step were fixed from $2\theta = 2^o$ to 118^o and 0.03^o/step, respectively, the conventional scan time was 3600 seconds per sample.

4.3 Scanning Electron Microscopy (SEM)

Powder samples were put into carbon film coated aluminum sample holders. Samples were coated with 10 nm gold in a Denton vacuum DESK II coater before the SEM measurement to avoid surface charging due to their low electronic property. A LEO 1530 field emission scanning electron microscope (FMSEM) instrument equipped with an energy dispersive X-ray spectroscopy (EDX) attachment was used for the high magnification measurement. Images were recorded at 10 kV with a backscattered electron detector.

4.4 Transmission Electron Microscopy (TEM)

Samples were supported on a 200 mesh Cu grid before the TEM measurement which used FEI TITAN 80-300HB Cubed as microscope. Images were recorded at 300 kV in TEM Bright Field mode.

4.5 Electrochemical measurements

Electrochemical measurements were carried out in coin-type cells using a commercial (MacPileTM) mutichannel galvanostatic/potentiostat operating in galvanostatic mode. The positive electrodes comprised 80 wt.% active material, 5 wt.% PVDF binder and 15 wt.% Super S carbon. The active material and super S were first mixed thoroughly in an agate mortar and pestle, and then dried in oven at 80^{o}C for 30 minutes. A solution mixture was prepared separately in which PVDF binder and N-Methyl-2-pyrrolidone were mixed in an agate mortar and pestle for 15 minutes. The mixture powder of active material and super S was mixed with the solution mixture in an agate mortar and pestle for 15 minutes. The slurry was spread onto a pre-weight 2 cm^2 carbon-coated aluminum disk by pipette. The coated disks were dried in a 120^{o}C vacuum oven for overnight. Cathode loadings were in the range of 5 - 6 mg cm^{-1} and electrode diameters of 16 mm were used throughout. The electrolyte was composed of a 1M $LiPF_6$ dissolved 1:1 ethylene carbonate (EC)/dimethyl carbonate (DMC) solution. Lithium metal was used as anode. All coin-type cells were assembled in a glove box under Ar with O_2 and H_2O lower than 5 ppm. The construction of a coin cell is shown in Figure 35.

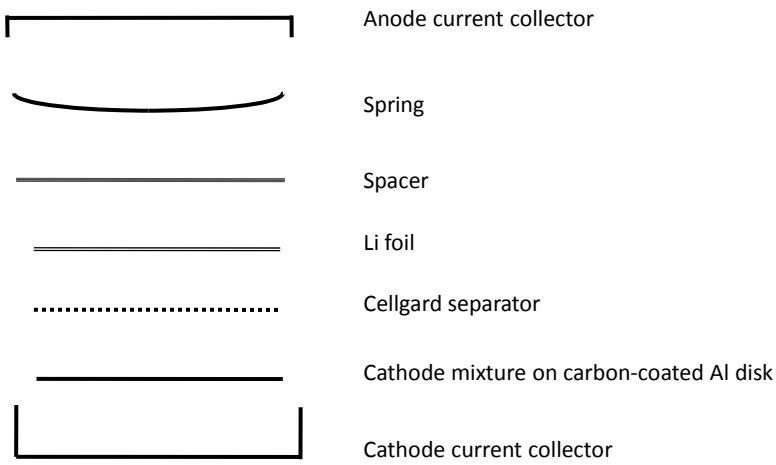

Figure 35: The construction of coin cells.

4.6 Thermogravimetric Analysis (TGA)

The TGA of the samples was carried out on a simultaneous TG-DTA apparatus SDT Q600 system (TA instruments) in oxygen or nitrogen (10°C/min; flow, 100 mL/min). Alumina or platinum crucibles were used as sample holders in the TGA measurements.

Chapter 5 Results and Discussions:

5.1 Hydrothermal synthesis

5.1.1 Study of the reaction mechanism

Hydrothermal synthesis is one of the most common methods used to prepare olivine $LiFePO_4$. Typically, micron-sized crystallites with diamond shapes are produced in the conventional method.[1] Moreover, synthesis of crystallites with other sized regimes and shapes has also been reported through the manipulation of experimental parameters, such as pH and reagents concentration.[2] However, the reaction mechanism remains unknown. Chemists rely on trial and error to obtain the desired crystal sizes and shapes. Probing the reaction mechanism would greatly facilitate the development of novel materials, thus motivating us to study the reaction mechanism through the careful analysis of reaction intermediates that are formed in the hydrothermal reactor.

Pure olivine $LiFePO_4$ can be prepared hydrothermally as noted in the equation below:

$$(NH_4)_2Fe(SO_4)_2 + H_3PO_4 + 3LiOH + 0.1 \text{ ascorbic acid} \xrightarrow{190^oC \quad 15\,h} LiFePO_4$$

Vivianite $Fe_3(PO_4)_2$ was first detected at room temperature when LiOH was added to the solution of H_3PO_4 and $(NH_4)_2Fe(SO_4)_2$ in the presence of small amounts of ascorbic acid. Hydrothermal synthesis of the solution mixture for 30 minutes converted all vivianite into an intermediate phase known as crystalline "nanoleaflets" characterized by X-ray diffraction. Nanoleaflets exhibit a relatively weak and disordered XRD pattern, with a strong reflection at

$2\theta = 9.8^{o}$. The intermediate phase decreased progressively, disappearing after 5 hours; at the same time, the $LiFePO_4$ phase increased gradually and became the only product.

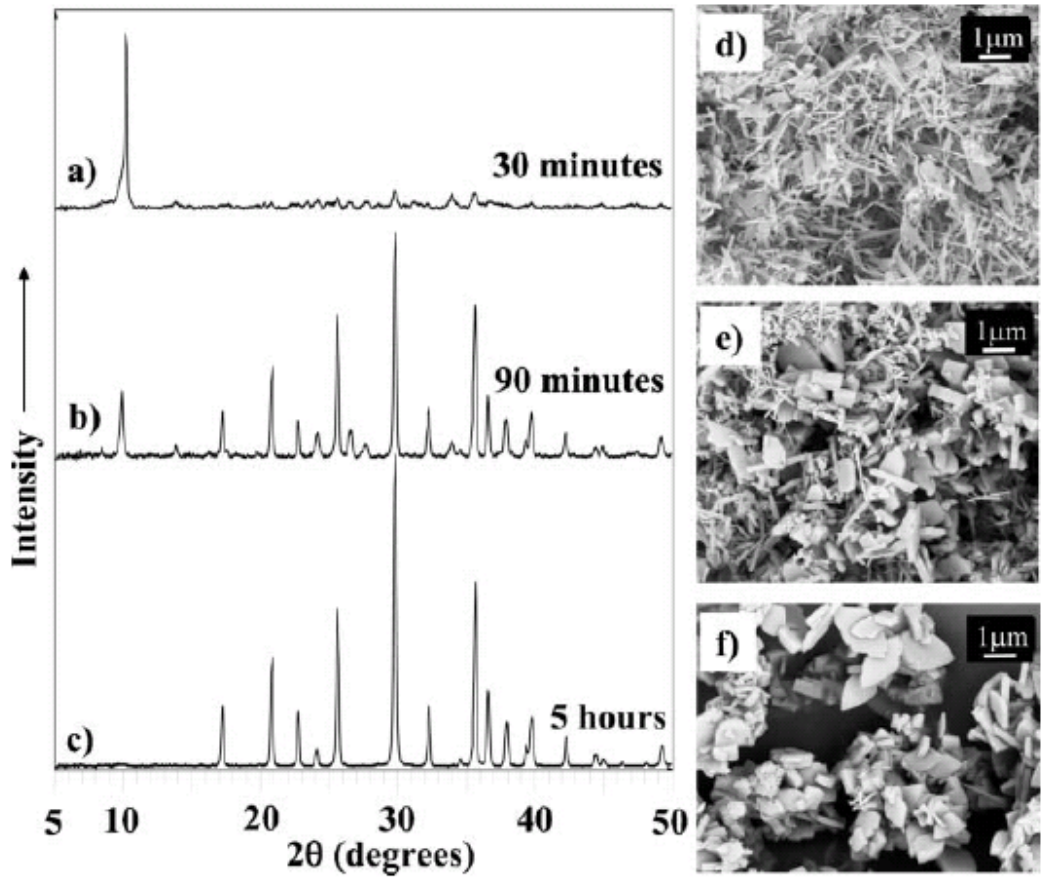

Figure 36: a), b) and c) show the XRD patterns of the products isolated from the hydrothermal reactors after 0.5 h, 1.5 h, and 5 h respectively; d), e), f) are the corresponding SEM images.

The XRD patterns of the intermediate in Figure 36a, and its morphology in Figure 36d, suggest that it may be related to $NH_4FePO_4 \cdot H_2O$ whose XRD pattern in Figure 37 is also dominated by a very prominent strong reflection at $2\theta = 9.8^{o}$ (JCDPS #45-0424). This corresponds to the (010) reflection in the *Pmn2₁* space group and the intensity is due to a high degree of preferred orientation arising from the thin plate morphology of this material.

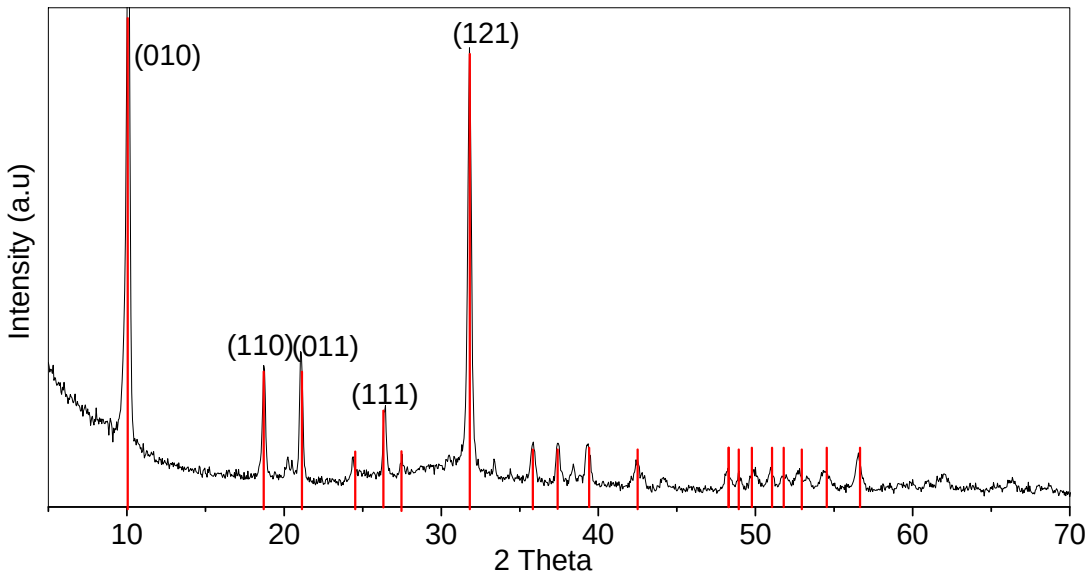

Figure 37: XRD pattern of $NH_4FePO_4 \cdot H_2O$.

A comparison of the structures of $LiFePO_4$ and $NH_4FePO_4 \cdot H_2O$ in Figure 38 indicates how they could be related by a simple transformation. The connectivity of the iron and phosphate polyhedral in the (100) plane (SG: *Pnma*) of $LiFePO_4$ is identical to that in the corresponding (101) plane (SG: $Pmn2_1$) of $NH_4FePO_4 \cdot H_2O$. Similarly, the d-spacing corresponding to the (020) reflection (SG: *Pnma*) in $LiFePO_4$ is almost the same as the (200) reflection (SG: $Pmn2_1$) for $NH_4FePO_4 \cdot H_2O$ since the repeating polyhedral motif is the same.

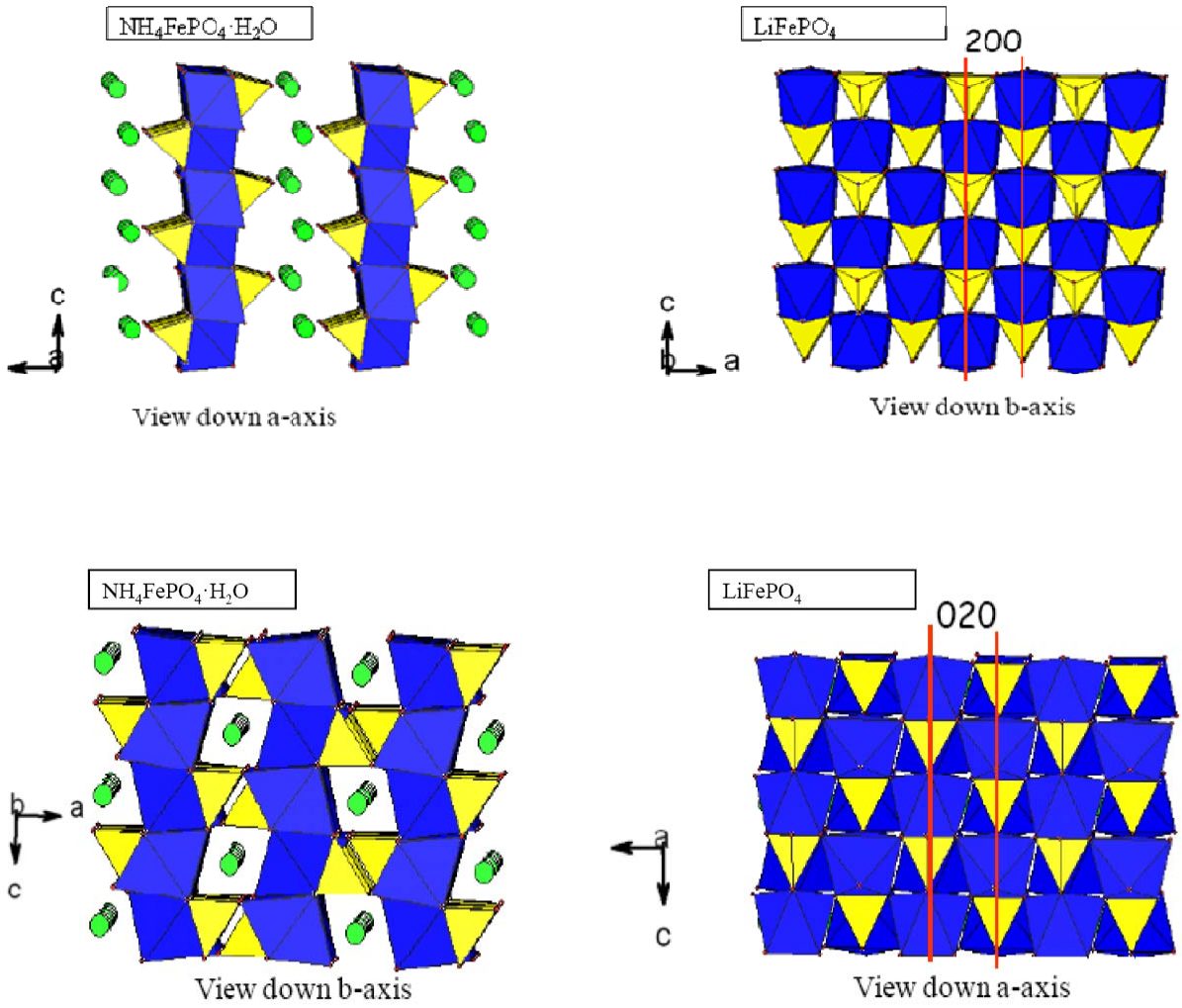

Figure 38: $NH_4FePO_4 \cdot H_2O$ and $LiFePO_4$ are structurally similar.

It is proposed that the precursors which initially precipitate in the autoclave (i.e. $Fe_3(PO_4)_2 \cdot 8H_2O$) are dissolved and react with NH_4^+ in the solution to form the ammonium intercalated solid $NH_4FePO_4 \cdot H_2O$. Upon rapid subsequent exchange of NH_4^+ and Li^+ in the autoclave solution, the adjacent sheets are condensed to the LiO_6 octahedra to crystallize $LiFePO_4$. The reaction intermediate that was observed after 30 minutes of reaction in the autoclave is clearly not exactly $NH_4FePO_4 \cdot H_2O$, but a material that has already undergone

partial Li^+ exchange to give rise to a disordered material. This is direct evidence from direct comparison of the XRD patterns of the intermediate and $NH_4FePO_4 \cdot H_2O$ which show a similarity but not an exact correspondence.

Further evidence of $NH_4FePO_4 \cdot H_2O$ being a possible reaction intermediate comes from the fact that it can be directly used as a precursor in the autoclave. The hydrothermal reaction of solid $NH_4FePO_4 \cdot H_2O$, LiOH and ascorbic acid readily produced single-phase $LiFePO_4$ with a unique tablet-shaped morphology. This is in contrast to the diamond-shaped morphology formed in conventional hydrothermal synthesis by Chen *et* al.[1] Small crystallites with basal dimensions of about 200 nm, and 100 nm thick were formed. Increasing the total concentration of the precursors yielded even smaller nanocrystallites with basal dimensions on the order of 50 nm.

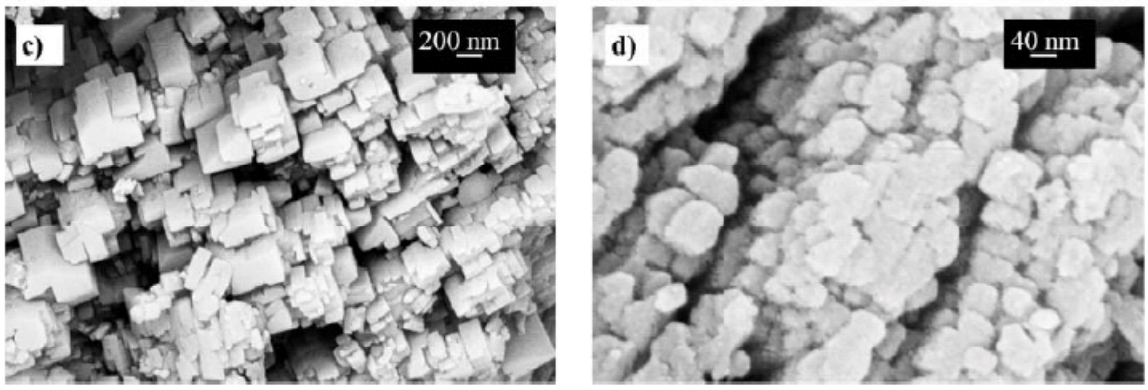

Figure 39: a) and b) SEM images of the $LiFePO_4$ nanocrystallites prepared from $NH_4FePO_4 \cdot H_2O$ precursor at concentration of 0.13 M and 0.4 M, respectively.

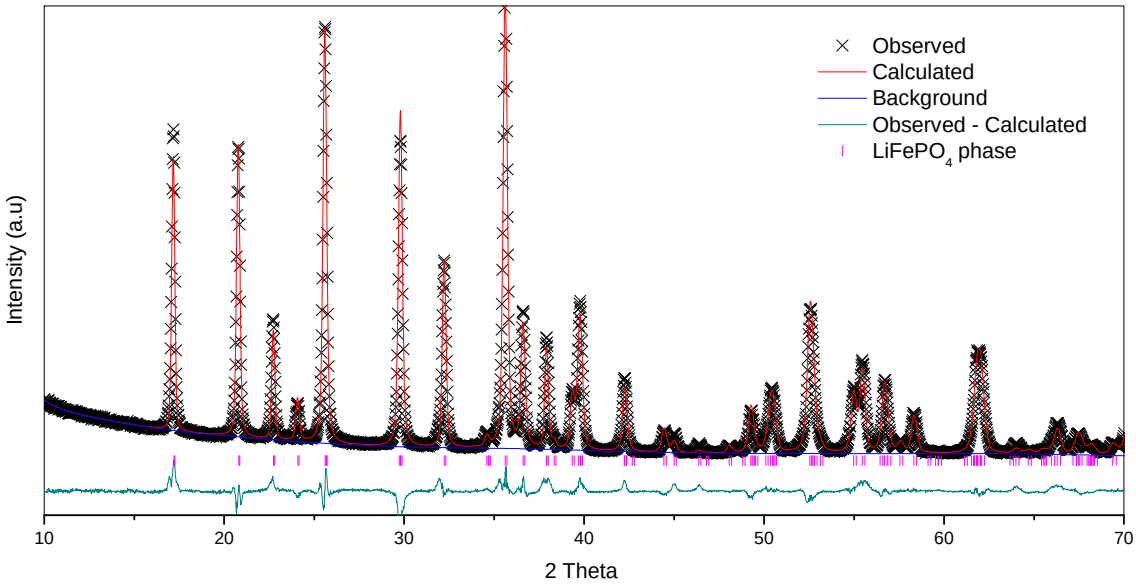

Figure 40: Rietveld refinement pattern of the $LiFePO_4$ nanocrystallites prepared from $NH_4FePO_4 \cdot H_2O$ precursor at concentration of 0.13 M.

Phase	Atom	Wyck.	x/a, y/b, z/c	$U_{iso}(100Å^2)$	Fraction
Pnma (62)	Li/Fe	4a	0, 0, 0	1.5	0.976(2)/0.024(2)
a = 10.3494(3) Å	Fe/Li	4c	0.2822(1),0.25, 0.9810(4)	2.3(1)	0.976(2)/0.024(2)
b = 6.0045(2) Å	P	4c	0.0974(3),0.25,0.4238(6)	4.1(1)	1
c = 4.7024(2) Å	O1	4c	0.1005(6), 0.25, 0.752(1)	2.9(1)	1
	O2	4c	0.4534(7), 0.25, 0.227(1)	2.9(1)	1
	O3	8d	0.1772(5), 0.0377(7), 0.2862(7)	2.9(1)	1
$_wR_p$ = 7.99, R_p = 5.99					

Table 7: Unit cell parameter and atom parameters resulting from simultaneous refinement of the X-ray data for the $LiFePO_4$ nanocrystallites prepared from $NH_4FePO_4 \cdot H_2O$ precursor at concentration of 0.13 M.

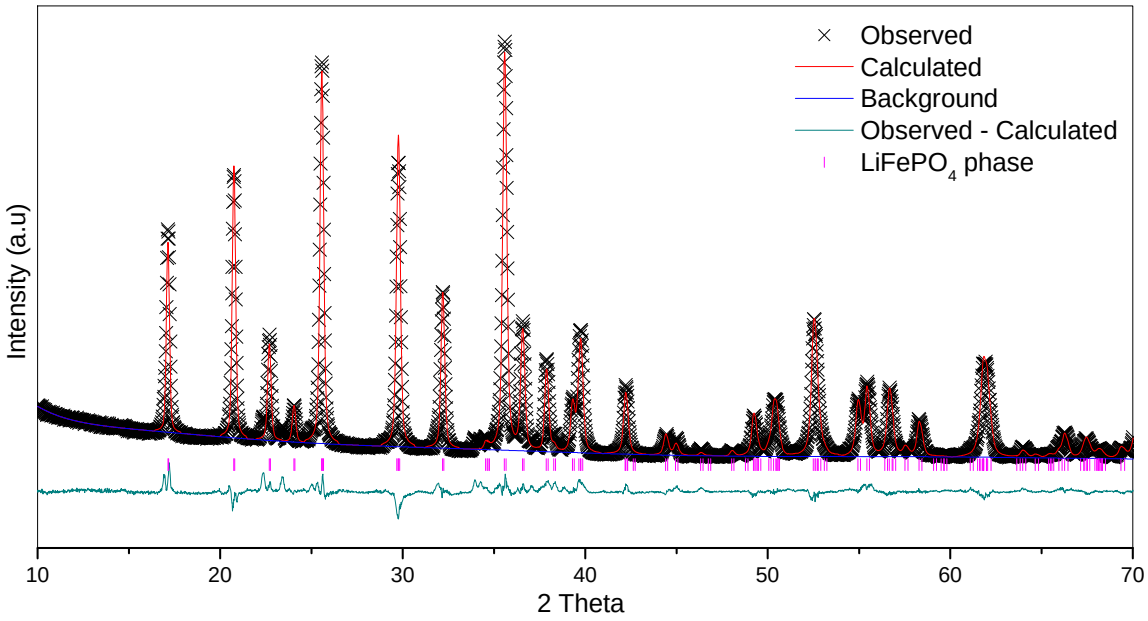

Figure 41: Rietveld refinement pattern of the $LiFePO_4$ nanocrystallites prepared from $NH_4FePO_4 \cdot H_2O$ precursor at concentration of 0.4 M.

Phase	Atom	Wyck.	x/a, y/b, z/c	$U_{iso}(100Å^2)$	Fraction
Pnma (62)	Li	4a	0,0,0	1.5	0.970(1)/0.030(1)
a = 10.3418(5) Å	Fe	4c	0.2820(1),0.25, 0.9772(3)	1.78(5)	0.970(1)/0.030(1)
b = 5.9997(3) Å	P	4c	0.0970(2),0.25,0.4212(4)	2.85(8)	1
c = 4.6993(2) Å	O1	4c	0.0980(5), 0.25, 0.7509(9)	2.80(8)	1
	O2	4c	0.4541(6), 0.25, 0.2166(9)	2.80(8)	1
	O3	8d	0.1721(5), 0.0408(6), 0.2845(6)	2.80(8)	1
$_wR_p$: 7.13, R_p: 5.74					

Table 8: Unit cell parameter and atom parameters resulting from simultaneous refinement of the X-ray data for the $LiFePO_4$ nanocrystallites prepared from $NH_4FePO_4 \cdot H_2O$ precursor at concentration of 0.4 M.

Our results suggest that particle shapes and sizes can also be modified through the choice of precursors in the reaction. If the precursor contains some structural similarity to the final product, those “building blocks” can be preserved and used to construct the product with the desired shape.

5.2 Polyol Process

5.2.1 Study of the effects of reagent concentrations on crystalline sizes

Phase pure $LiFePO_4$ nanocrystallites were prepared from polyol process in which $Fe(OAc)_2$ concentration of 0.25M was used. As a comparison, another batch of nanocrystalites was prepared at a lower concentration condition (0.02 M of $Fe(OAc)_2$ in tetraethylene glycol) to study of the effect of reagent concentration on crystalline size. The samples were purified and analyzed by XRD to determine their purity and crystallinity. The XRD patterns of the corresponding products in Figure 42 confirm that phase pure samples were prepared from two different concentrations of reagents. Additionally, weaker and broader diffraction peaks were observed from the sample prepared from the lower reagent concentration, thus indicating that smaller crystallites were obtained at lower concentrations.

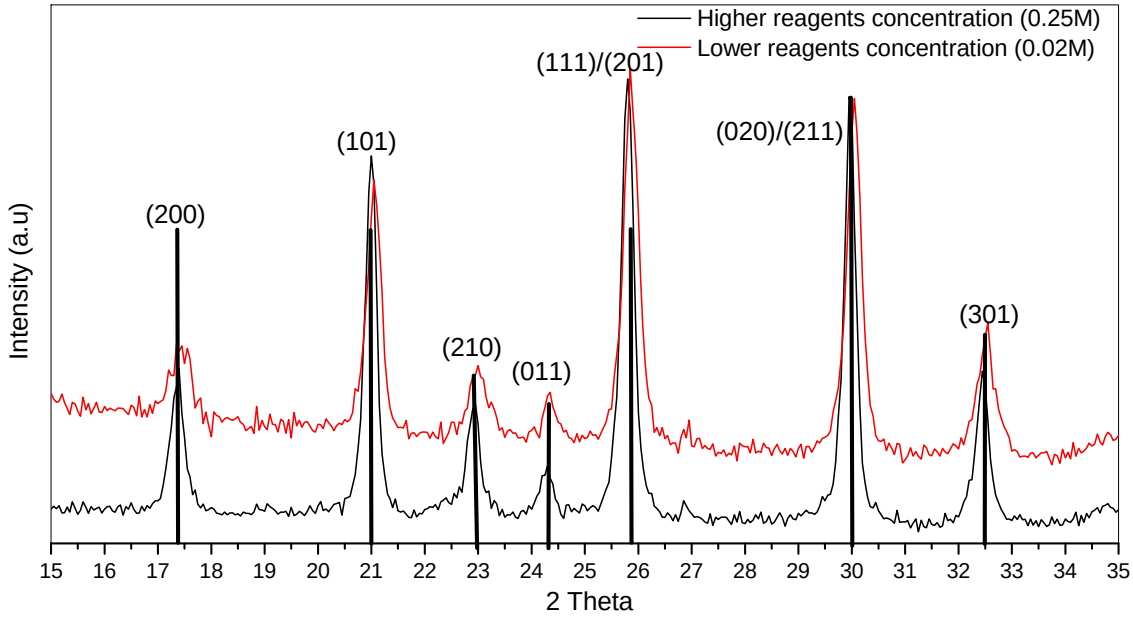

Figure 42: XRD patterns of the $LiFePO_4$ nanocrystallties prepared from different reagents concentration; black solid line represents the sample prepared from higher reagent concentration (0.25M of $Fe(OAc)_2$ in tetraethylene glycol), red solid line represents the same prepared from lower reagent concentration (0.02M of $Fe(OAc)_2$ in tetraethylene glycol).

The coherence lengths along [200] and [020] directions of the crystallites were calculated from the full width at half-maximum (FWHM) values of selected diffraction lines of the XRD corresponding patterns by the Scherrer formula to quantitatively estimate the sizes of crystallites; this is summarized in Table 9. The results show that the crystallites were anisotropic with certain shorter (a few tenths of a nanometer) dimensions.

Various reagents Concentration	FWHM (200)	Coherence length [200]	FWHM (020)	Coherence length [020]
0.25 M	0.301 ± 0.03^{o}	26 ± 3 nm	0.264 ± 0.03^{o}	31 ± 3 nm
0.02 M	0.455 ± 0.05^{o}	17 ± 2 nm	0.343 ± 0.03^{o}	23 ± 3 nm

Table 9: Peak widths and coherence lengths of the corresponding samples are shown.

The coherence lengths along [200] and [020] reduced by 34% and 23%, respectively, when the reagents concentration was diluted about 10 times, indicating that the formation of the amount of nucleation sites is relatively independent of the reagents concentration. However, lower reagents concentration conditions could reduce the crystal growth rate, yielding smaller crystallites. The schematic diagram in Figure 43 shows how the reagents concentration affects the morphology.

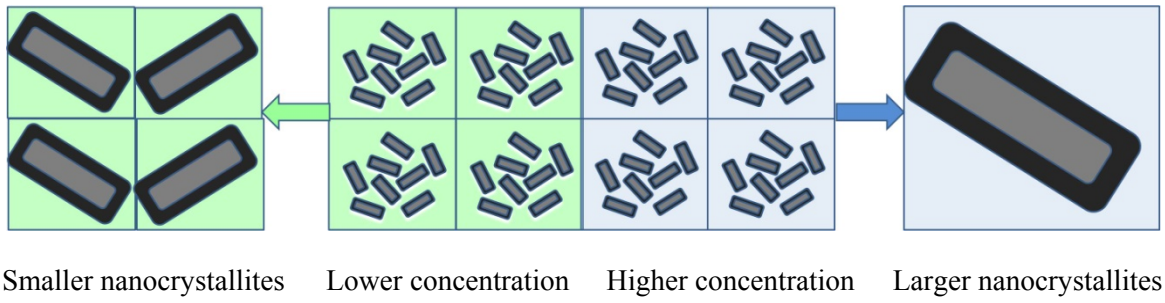

Figure 43: Schematic diagram showing the effect of the change of reagents concentration on the size of nanocrystallites; green and blue colors represent low and high concentration conditions, respectively.

To conclude, nanocrystalline dimensions can be controlled through the manipulation of reagent concentration. Smaller nanocrystallites can be synthesized at a lower concentration of reagent. Formation of nucleation sites is relatively independent of the reagent concentration range under investigation. However a higher concentration of reagent environment can promote a faster rate of crystal growth. Reduction of crystalline dimensions, especially along [020] direction, could

shorten the lithium ions diffusion length, and therefore minimize the diffusion time. Moreover reduction of crystalline dimensions could also increase accessibility to the electrolyte, so as to improve the rate capability.

5.2.2 Study of the effects of reaction times on crystalline sizes

Nanocrystallites were prepared from various lengths of refluxing times to study the effect of reaction time on crystalline size. Several reactions were set up in the same reagents concentration (0.0625 M of $Fe(OAc)_2$ in tetraethylene glycol) under reflux conditions for various lengths of time. Samples were purified and characterized by XRD and TEM to determine their purity and particle size.

Interestingly, phase pure samples could be prepared under the reflux condition for just 3 hours, which was much shorter than the conventional time reported by Kim and coworkers.[3] As large amounts of impurities were detected when the reaction time was shorter than 3 hours, reaction does not appear to be completed when the refluxing time is too short.

We also observed from the TEM images that decreasing the reaction time from 20 to 3 hours, at the same reagent concentrations, yielded homogeneous nanocrystallites with smaller dimensions. The corresponding TEM images in Figure 44 and Figure 45 show that 25 X 100 nm nanorods and 15 X 50 nm nanoneedles were obtained in 20 hours and 3 hours, respectively. Shortening the reaction time from 20 hours to 3 hours did not generally affect the crystalline shapes; apparently, they all have anisotropic growth direction to form nanorods or nanoneedles.

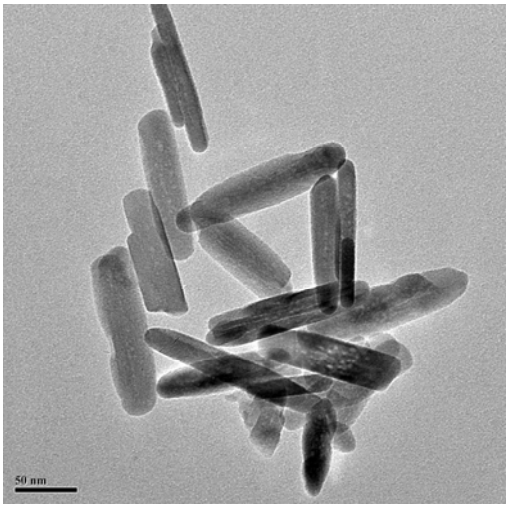

Figure 44: TEM image of the 20 h $LiFePO_4$ samples.

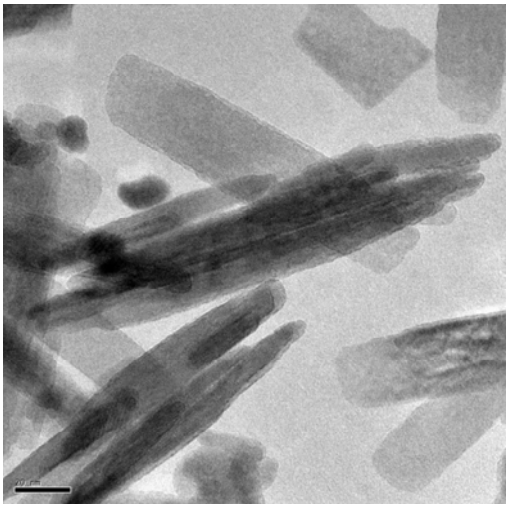

Figure 45: TEM image of the 3 h $LiFePO_4$ samples.

The corresponding XRD patterns, see Figure 47, show that phase pure olivine samples were obtained from various lengths of reaction times; from 3 hours, 6 hours and 20 hours. Average crystalline sizes were estimated through the calculations of the Scherrer equation from the full width at half-maximum (FWHM) values of most of the diffraction lines of the XRD corresponding patterns.

Various reaction time	FWHM (200)	Coherence length [200]	FWHM (020)	Coherence length [020]
3 h LFP sample	0.59 ± 0.06^o	13 ± 2 nm	0.38 ± 0.04^o	21 ± 2 nm
6 h LFP sample	0.48 ± 0.05^o	16 ± 2 nm	0.36 ± 0.04^o	22 ± 3 nm
9 h LFP sample	0.47 ± 0.05^o	17 ± 2 nm	0.31 ± 0.03^o	26 ± 3 nm
20 h LFP sample	0.38 ± 0.04^o	21 ± 2 nm	0.33 ± 0.03^o	24 ± 3 nm

Table 10: Summary of the effect of reaction times on $LiFePO_4$ crystalline sizes; crystallites with shorter coherence lengths were obtained from lower reagent concentrations.

The corresponding coherence lengths along [200] and [020] directions for the samples prepared in 20 hours and 3 hours agreed with the shortest dimensions observed from the TEM images indicating that the nanocrystallites formed in the polyol process are single crystals. Moreover, it suggests that anisotropic growth orientation could be in the [002] direction, which is perpendicular to the [020] and [200] directions. Since the relative intensity from the (002) plane was very weak, we were not able to measure the precise coherence lengths from the FWHM values to confirm.

When the reaction time was shortened from 20 hours to 3 hours, the coherence lengths along [200] and [020] directions (SG: *Pnma*) were reduced by about 35% and 14%, respectively, thus indicating that the crystal growth process was reduced when the reaction time was shortened which yielded smaller nanocrystallties as shown in Figure 46.

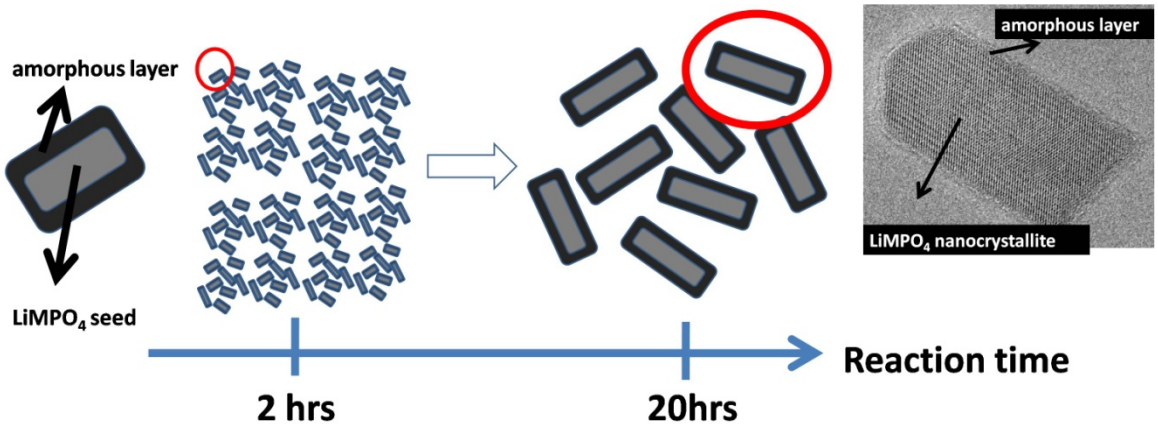

Figure 46: Crystal growth process is minimized when the reaction time is shortened.

Moreover, broaden diffraction peaks were observed when the reaction time was reduced. That indicates that the coherence length along every direction was generally shortened. This reduction, especially along [020] direction, is significant to improving the accessibility of active materials to electrolytes, and reducing the lithium ions diffusion distance which could be beneficial for electrochemical performances especially to the rate capability.

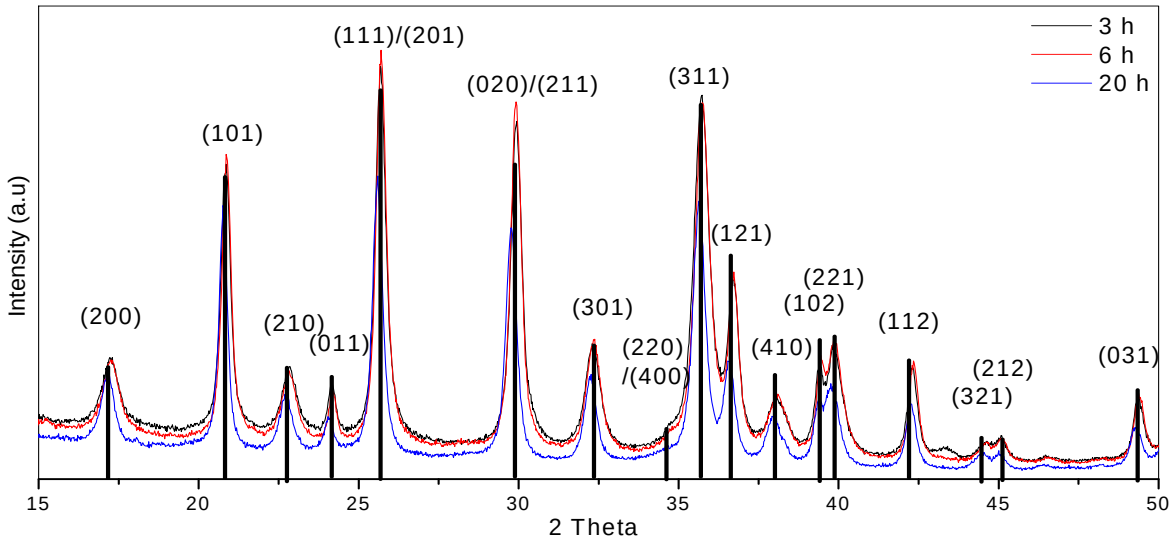

Figure 47: XRD patterns of the corresponding $LiFePO_4$ nanocrystallites prepared from various length of reaction time.

5.2.3 Comparison of unit cell volumes and cell parameters of various sizes of $LiFePO_4$ nanocrystallies

Decrease in unit cell volume for $LiFePO_4$ particles with sizes small than 100 nm has been reported earlier.[3,4,5,6,7] Ellis and coworkers discussed that the reduction was likely similar to that seen in oxide of iron (γ-Fe_2O_3) and cobalt (Co_3O_4) in which the decrease in lattice parameters was attributed to strain on the particles as a result of high surface tension.[6,8,9] On the other hand, Masquelier group suggested that the reduction could be caused by the present of lithium vacancies linked to an increase in Fe^{3+} in the lattice. They observed a significant reduction in cell volume (V = 289.1 $Å^3$) in their 40 nm nanocrystalline samples by 0.7% (comparing with the conventional one), in which 15% of lithium vacancies were estimated by chemical analyses and Rietveld refinement of XRD data, and 22% of Fe^{3+} was deduced by both chemical titration analysis and Mössbauer.[10] Nonetheless such reduction in the cell volume (V = 291.2 $Å^3$) was not observed in their 140 nm nanocrystallies, in which 12% of Fe^{3+} was estimated in the lattice.[10] Their results suggest there could be other factors to affect the unit cell volume other than the present of lithium vacancies and Fe^{3+} ions, for example the present of Fe mixing/disorder in the lattice. It is evident from their Rietveld refinement results that 4% and 6% of iron were detected in the lithium site in their 140 nm and 40 nm nanocrystallites respectively. Such a Fe mixing/disorder in $LiFePO_4$ crystallites was also reported earlier.[1,10,11] It was reported by Chen and coworkers that ca. 6% of iron was in lithium site estimated through XRD Rietveld analysis in their hydrothermal $LiFePO_4$ samples, in which a larger unit cell volume was observed.[1,11] Moreover no trace amount of Fe^{3+} was detected in their hydrothermal samples by titration method.[1] A systematical comparison of unit

cell volume and the amount of Fe mixing/disorder was later conducted by Chen and coworkers showing that the present of Fe mixing/disorder in the lattice did result in increasing the unit cell volume,[12] considering that the size of Fe^{2+} (r_{ion} = 0.78 Å) is slightly bigger than Li^{+} (r_{ion} = 0.76Å).

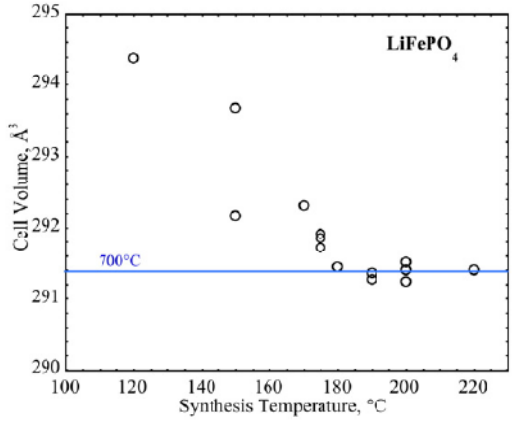

Figure 48: Unit cell volume of $LiFePO_4$ is highly affected by the synthesis temperature in the hydrothermal synthesis.[12]

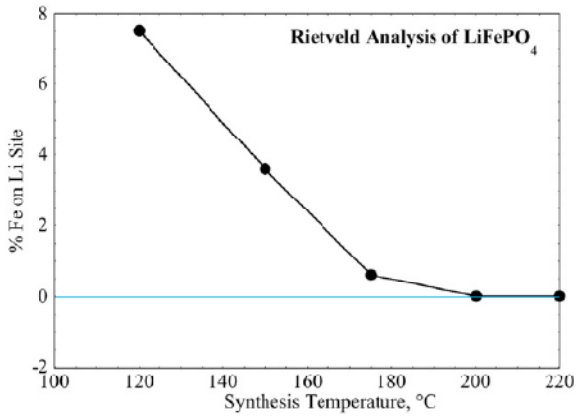

Figure 49: The amount of anti-site mixing can be reduced by using higher synthesis temperature, in the hydrothermal synthesis of $LiFePO_4$.[12]

Those results described above indicate that the unit cell volume is not changed by reducing the particle sizes along; more importantly the alternation of cell volume comes from the combination effects of the amount of lithium vacancies, Fe^{3+} concentration, Fe mixing/disorder and particle sizes. Conventional Rietveld methods using the GSAS package with the EXPGUI interface were used to refine the X-ray datasets of our various sizes of $LiFePO_4$ nanocrystallies prepared from the polyol process. The X-ray refinement patterns were shown in Figure 50, Figure 51, Figure 52, and Figure 53; those cell volume, lattice parameters and anti-site mixing data were summarized in Table 11, Table 12, Table 13, Table 14, and Table 15.

From the refinement results, no significant reduction of the unit cell volumes and lattice parameters were observed from all of our nano-sized (below 100 nm) crystallites; those values were consistent with previous reports.[13,14] It is evident that the reduction of unit cell parameters and change of lattice parameters in $LiFePO_4$ nanocrystallites are not simply correlated to the crystalline sizes. Moreover uncertain small amount (ca. 1 – 3%; below the detection limit of XRD) of Fe was found in lithium site (anti-site disorders) in our nanocrystallites analyzed through X-ray Rietveld refinements. Nonetheless no significant increase of the unit cell volume was observed in those sample as opposed to Chen and coworkers observed earlier.[1] The amount of anti-site disorder in our samples was similar to the 140 nm nanocrystallies (4% Fe in lithium site) prepared by Masquelier and coworker in which no reduction in unit cell volume was observed in their samples. That suggests if there are some lithium vacancies sites, or Fe^{3+} ions present in our samples. However X-ray diffraction is not so sensitive to measure light atoms with weak scattering power, for example the lithium atom. Precise measurements, without significant errors, of the lithium vacancies by X-ray diffraction cannot be done. Perhaps Rietveld refinement using X-ray and neutron diffractions data could be the most accurate method to address the lithium vacancies.

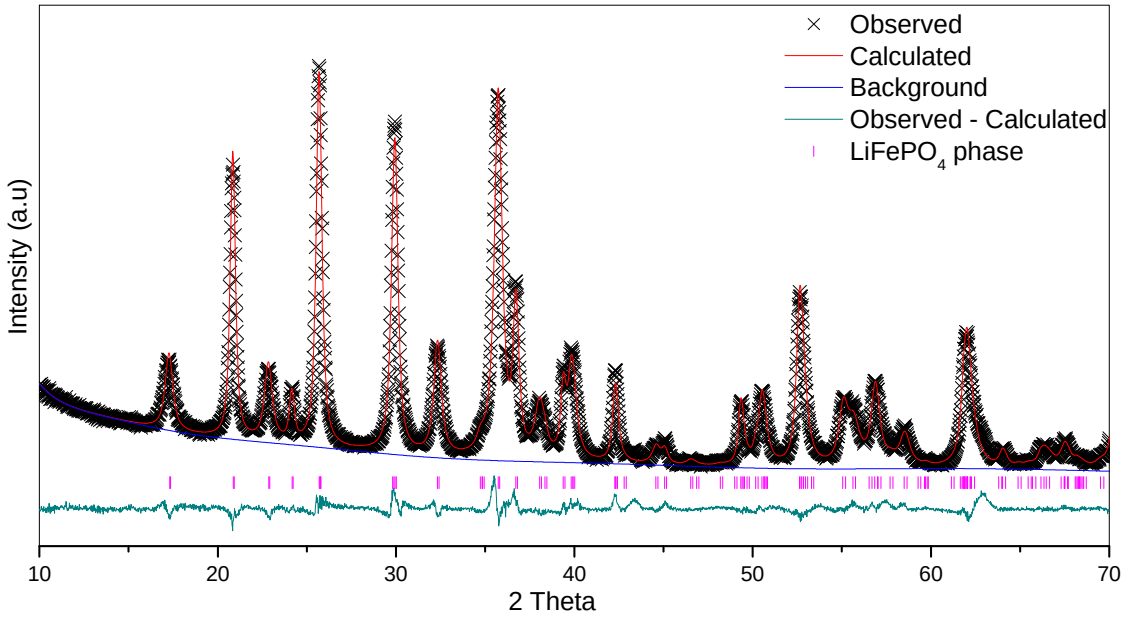

Figure 50: XRD Rietveld refinement pattern of the 3 h $LiFePO_4$ samples.

Phase	Atom	Wyck.	x/a, y/b, z/c	$U_{iso}(100Å^2)$	Fraction
Pnma (62)	Li/Fe	4a	0,0,0	1.5	0.968(1)/0.032(1)
a = 10.332(1) Å	Fe/Li	4c	0.2807(1),0.25, 0.9732(3)	1.73(6)	0.968(1)/0.032(1)
b = 5.9925(5) Å	P	4c	0.0945(2),0.25,0.4204(4)	2.62(8)	1
c = 4.7075(3) Å	O1	4c	0.0945(6), 0.25, 0.7323(9)	2.57(8)	1
	O2	4c	0.4496(6), 0.25, 0.2246(9)	2.57(8)	1
	O3	8d	0.1596(4), 0.0500(5), 0.2830(5)	2.57(8)	1
$_wR_p$: 5.87, R_p: 4.39					

Table 11: Unit cell parameter and atom parameters resulting from simultaneous refinement of the X-ray data for the 3 h $LiFePO_4$ samples.

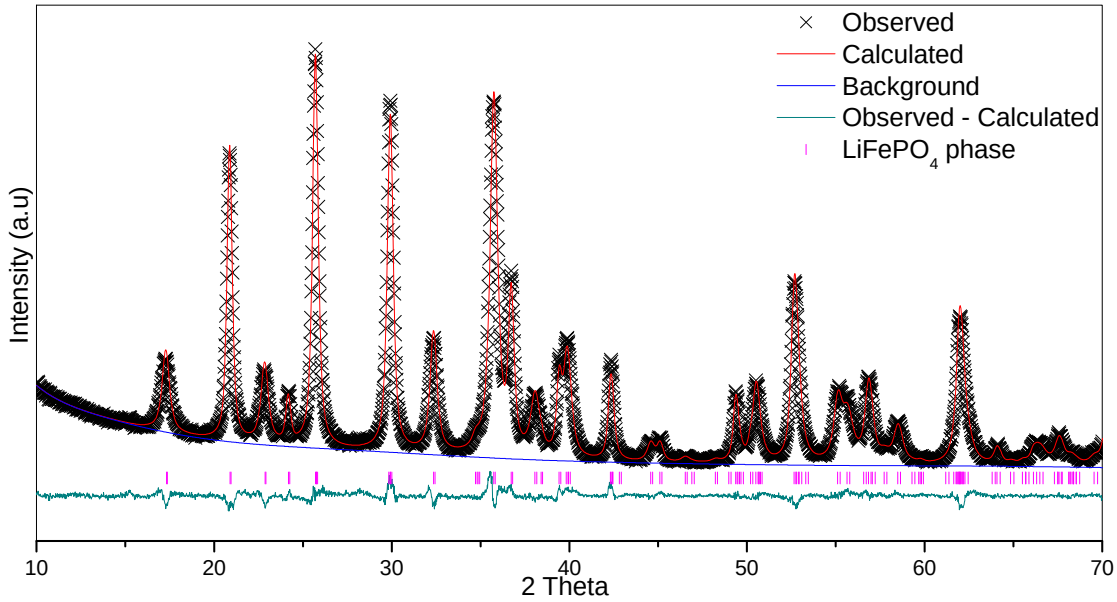

Figure 51: XRD Rietveld refinement pattern of the 6 h $LiFePO_4$ samples.

Phase	Atom	Wyck.	x/a, y/b, z/c	$U_{iso}(100Å^2)$	Fraction
Pnma (62)	Li/Fe	4a	0,0,0	1.5	0.969(1)/0.031(1)
a = 10.3319(7)Å	Fe/Li	4c	0.2817(1),0.25, 0.9730(2)	1.83(4)	0.969(1)/0.031(1)
b = 5.9979(4) Å	P	4c	0.0947(2),0.25,0.4202(3)	2.73(6)	1
c = 4.7037(3) Å	O1	4c	0.0950(4), 0.25, 0.7415(6)	2.17 (6)	1
	O2	4c	0.4536(5), 0.25, 0.2157(6)	2.17 (6)	1
	O3	8d	0.1620(3), 0.0490(4), 0.2831(4)	2.17 (6)	1
$_wR_p$: 4.93, R_p: 3.95					

Table 12: Unit cell parameter and atom parameters resulting from simultaneous refinement of the X-ray data for the 6 h $LiFePO_4$ samples.

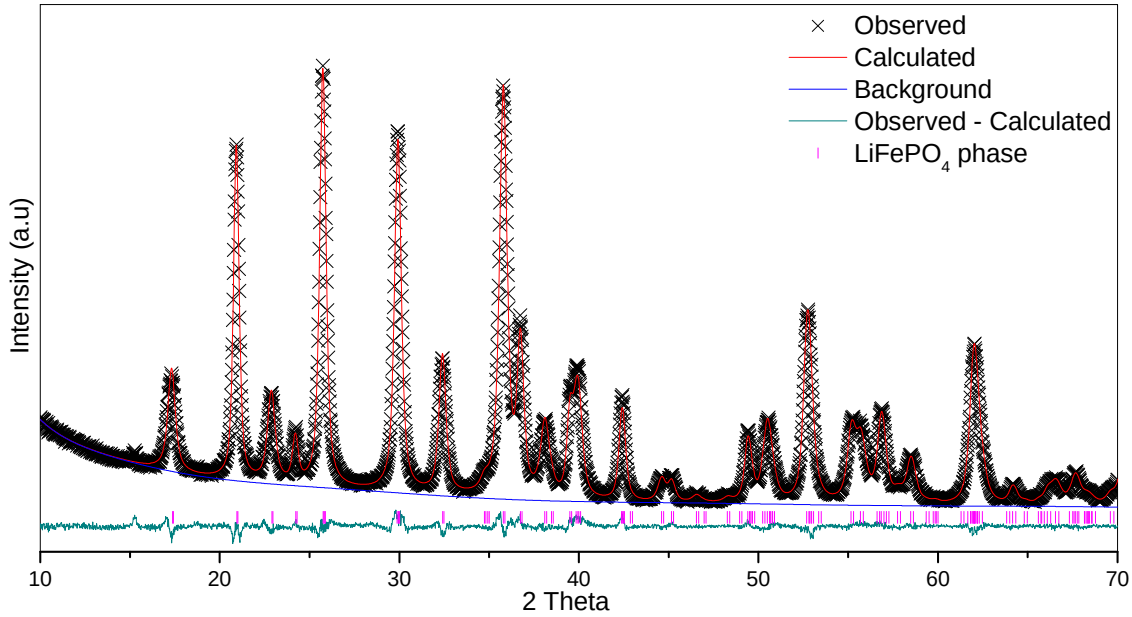

Figure 52: XRD Rietveld refinement pattern of the 9 h $LiFePO_4$ samples.

Phase	Atom	Wyck.	x/a, y/b, z/c	$U_{iso}(100Å^2)$	Fraction
Pnma (62)	Li/Fe	4a	0,0,0	1.5	0.983(1)/0.017(1)
a = 10.3307(6) Å	Fe/Li	4c	0.2820(1),0.25, 0.9724(2)	2.00(4)	0.981(1)/0.017(1)
b = 6.0054(3) Å	P	4c	0.0952(1),0.25,0.4199(3)	2.48(5)	1
c = 4.7006(2) Å	O1	4c	0.0943(3), 0.25, 0.7441(5)	2.03(5)	1
	O2	4c	0.4552(4), 0.25, 0.2130(6)	2.03(5)	1
	O3	8d	0.1628(3), 0.0499(4), 0.2831(3)	2.03(5)	1
$_wR_p$: 4.38, R_p: 3.44					

Table 13: Unit cell parameter and atom parameters resulting from simultaneous refinement of the X-ray data for the 9 h $LiFePO_4$ samples.

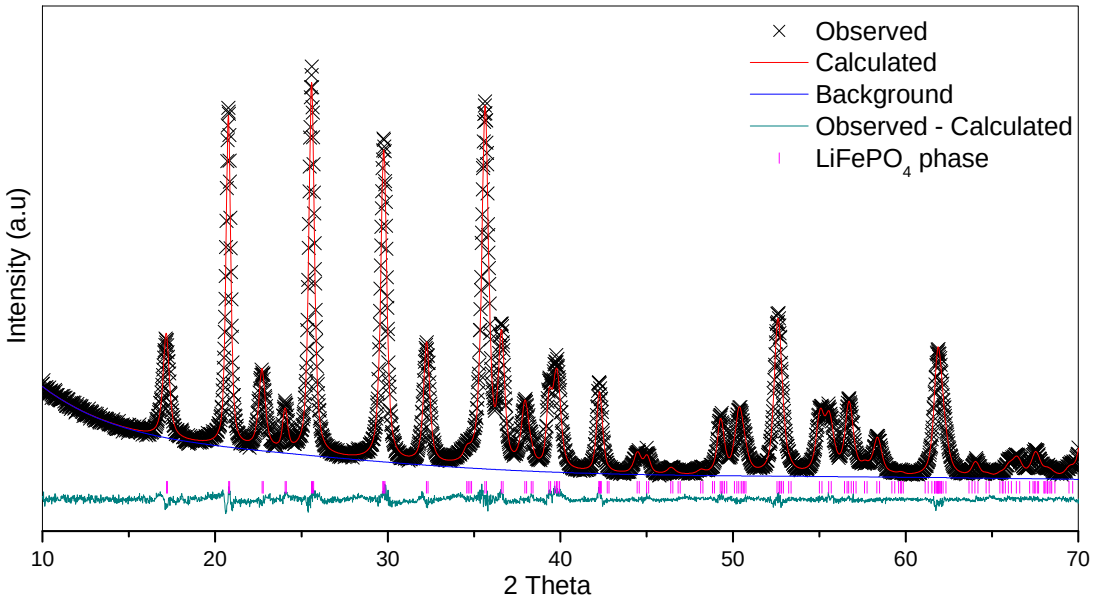

Figure 53: XRD Rietveld refinement pattern of the 20 h $LiFePO_4$ samples.

Phase	Atom	Wyck.	x/a, y/b, z/c	$U_{iso}(100Å^2)$	Fraction
Pnma (62)	Li/Fe	4a	0,0,0	1.5	0.995(1)/0.005(1)
a = 10.3233(6) Å	Fe/Li	4c	0.2817(1),0.25, 0.9733(2)	2.13(5)	0.995(1)/0.005(1)
b = 6.0022(4) Å	P	4c	0.0958(2),0.25,0.4200(3)	2.88(7)	1
c = 4.6978(3) Å	O1	4c	0.0942(4), 0.25, 0.7380(7)	2.19(6)	1
	O2	4c	0.4540(5), 0.25, 0.2100(7)	2.19(6)	1
	O3	8d	0.1620(3), 0.0500(4), 0.2830(4)	2.19(6)	1
$_wR_p$: 4.58, R_p: 3.76					

Table 14: Unit cell parameter and atom parameters resulting from simultaneous refinement of the X-ray data for the 20 h $LiFePO_4$ samples.

Various sizes of $LiFePO_4$ nanocrystallites	Cell volume /$Å^3$	a /Å	b /Å	c /Å
13 ± 2 nm (3 h LFP sample)	291.46(7)	10.3318(9)	5.9925(5)	4.7075(3)
16 ± 2 nm (6 h LFP sample)	291.49(5)	10.3319(7)	5.9979(4)	4.7037(3)
17 ± 2 nm (9 h LFP sample)	291.62(4)	10.3307(6)	6.0054(3)	4.7006(2)
21 ± 2 nm (20 h LFP sample)	291.09(5)	10.3233(6)	6.0022(4)	4.6978(3)

Table 15: Comparison of unit cell volumes and cell parameters of various sizes of $LiFePO_4$ nanocrystallites.

Sample	Cell volume /$Å^3$	a /Å	b /Å	c /Å
21 ± 2 nm $LiFePO_4$ (20 h LFP sample)	291.09(5)	10.3233(6)	6.0022(4)	4.6978(3)
21 ± 2 nm $FePO_4$ (20 h FP sample)	272.0(1)	9.898(1)	5.793(1)	4.782(1)
Micron-sized $LiFePO_4$ Goodenough *et al.*[13]	291.392(3)	10.334(4)	6.008(3)	4.691(1)
Micron-sized $FePO_4$ Goodenough *et al.*[13]	272.357(1)	9.821(1)	5.792(1)	4.788(1)

Table 16: Comparison of unit cell volumes and cell parameters of the lithiated and delithiated phases $LiFePO_4$ and $FePO_4$ prepared from polyol process.

5.2.4 Study of the same experimental techniques and methodologies on other olivine members $LiMPO_4$ (M = Mn and Co) for the morphology control

5.2.4.1 Synthesis of pure polyol $LiMnPO_4$ nanocrystallites

In the previous chapter, we demonstrated the morphology control of $LiFePO_4$ in the polyol process. We extended the study to other olivine members $LiMPO_4$ (M = Mn and Co) to see whether the same experimental techniques and methodologies could be applied to synthesize nanocrystallites with different sizes, thus improving their conductivities and electrochemical performances.

$LiMnPO_4$ nanocrystallites were synthesized using $Mn(OAc)_2$, LiOAc, and H_3PO_4 as precursors and under reflux condition in tetraethylene glycol (TEG) for 20 hours. The corresponding XRD refinement pattern in Figure 54 shows that an olivine $LiMnPO_4$ phase pure sample was made without the presence of other impurities. An elemental measurement on the $LiMnPO_4$ sample by energy dispersive X-ray spectroscopy (EDS) in Figure 56 confirmed a 1:1:4 molar ratio of Mn:P:O. The corresponding TEM image in Figure 55 shows that $LiMnPO_4$ nanocrystalline sizes were very homogeneous with dimensions 50 nm width and up to 100 nm long. To the best of our knowledge, the $LiMnPO_4$ nanocrystallites made in our lab are the smallest $LiMnPO_4$ nanocrystallties ever reported in polyol process. Synthesis of the second smallest $LiMnPO_4$ nanocrystallites in polyol process was reported by Kim and coworkers.[15]

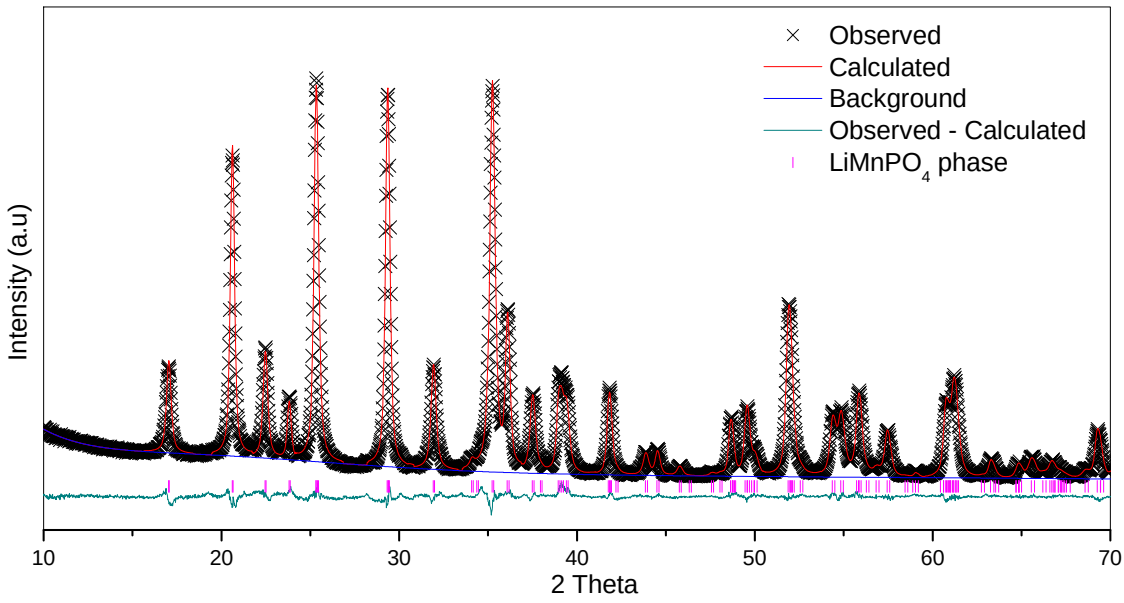

Figure 54: XRD Rietveld refinement pattern of the 20 h $LiMnPO_4$ samples.

Phase	Atom	Wyck.	x/a, y/b, z/c	$U_{iso}(100Å^2)$	Fraction
Pnma (62)	Li	4a	0,0,0	1.5	1.00
a = 10.4599(5) Å	Mn	4c	0.2817(6),0.25, 0.9708(2)	2.34(5)	1.00
b = 6.1065(3) Å	P	4c	0.0935(1),0.25,0.4108(3)	2.74(7)	1.00
c = 4.7518(2) Å	O1	4c	0.0934(3), 0.25, 0.7293(6)	1.64(6)	1.00
	O2	4c	0.4540(4), 0.25, 0.2118(5)	1.64(6)	1.00
	O3	8d	0.1590(2), 0.0553(3), 0.2761(4)	1.64(6)	1.00
$_wR_p$: 3.70, R_p: 2.97					

Table 17: Unit cell parameter and atom parameters resulting from simultaneous refinement of the X-ray data for the 20 h $LiMnPO_4$ samples.

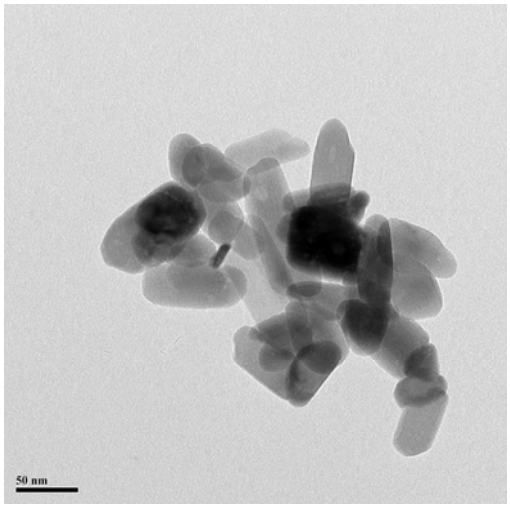

Figure 55: TEM image of the 20 h $LiMnPO_4$ samples.

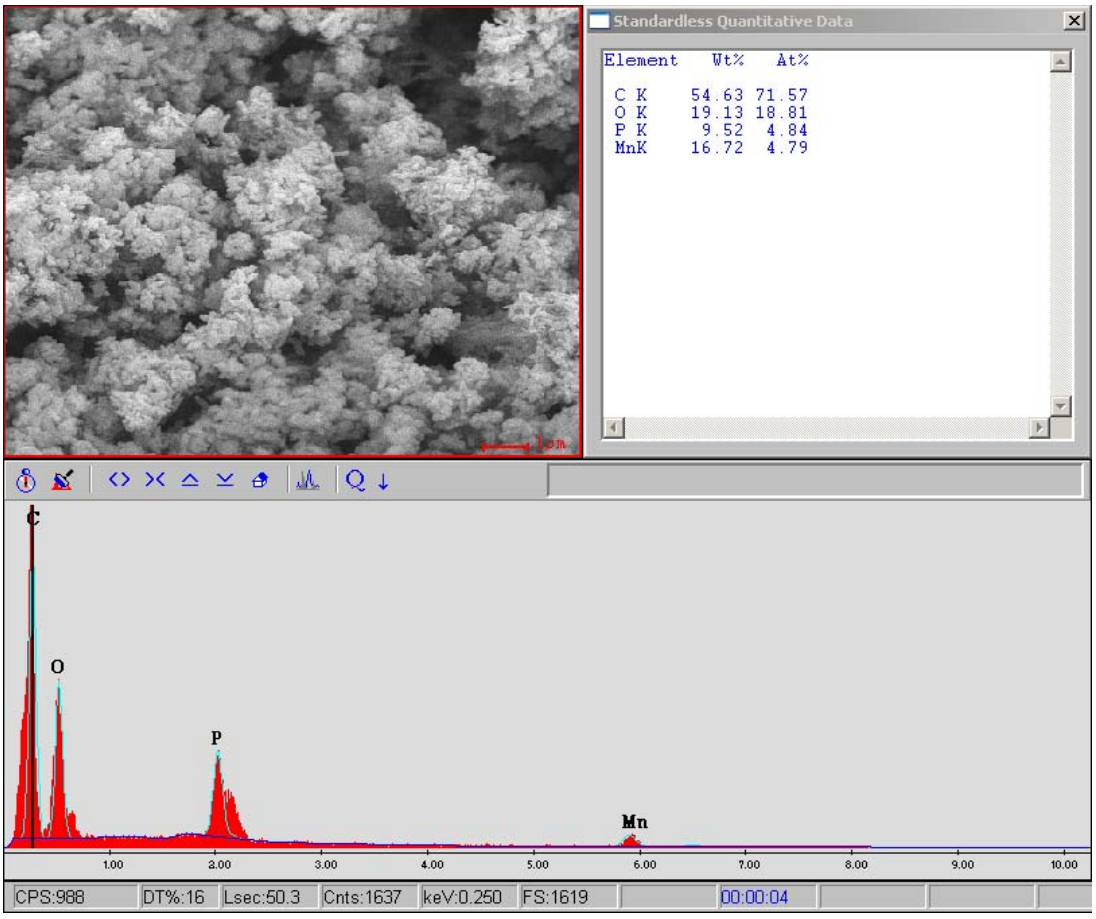

Figure 56: Elemental analysis by energy dispersive spectrum confirms the correct molar ratio among Mn, P, and O in the 20 h $LiMnPO_4$ samples.

5.2.4.2 Effect on reaction times on $LiMnPO_4$ nanocrystalline sizes

$LiMnPO_4$ crystallites were synthesized at shorter reaction times from 20 hours to 3 hours. The corresponding XRD pattern in Figure 57 confirms that fairly pure (with very small impurities) $LiMnPO_4$ crystallites were synthesized in 3 hours.

Although the reduction was relatively small in the polyol $LiMnPO_4$ reactions, a reduction of coherence lengths was observed as the reaction time was shortened. The coherence lengths along [200] and [020] direction reduced about 5% and 10%, respectively, when the reflux duration was shortened from 20 hours to 3 hours as shown in Table 19. The result suggests that the rate of crystal growth process of $LiMnPO_4$ is much faster than that of $LiFePO_4$. This can be further confirmed by the corresponding TEM image of $LiMnPO_4$ prepared in 3 hours in Figure 58; the particle sizes between $LiMnPO_4$ prepared in 20 hours and 3 hours were fairly similar.

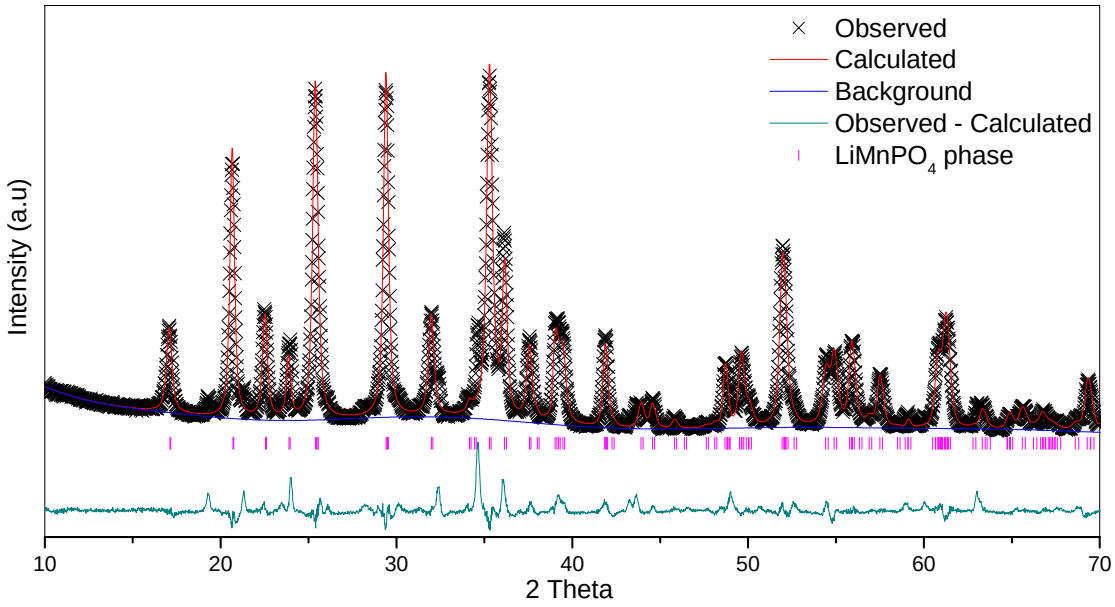

Figure 57: XRD refinement pattern of the 3 h $LiMnPO_4$ samples.

Phase	Atom	Wyck.	x/a, y/b, z/c	$U_{iso}(100Å^2)$	Fraction
Pnma (62)	Li	4a	0,0,0	1.5	1.00
a = 10.463(1) Å	Mn	4c	0.2819(2),0.25, 0.9716(5)	2.0(1)	1.00
b = 6.1077(8) Å	P	4c	0.0954(4),0.25,0.4120(8)	2.7(2)	1.00
c = 4.7534(6) Å	O1	4c	0.0912(8), 0.25, 0.730(2)	1.1(2)	1.00
	O2	4c	0.4477(9), 0.25, 0.212(1)	1.1(2)	1.00
	O3	8d	0.1575(6), 0.0612(8), 0.2691(9)	1.1(2)	1.00
$_wR_p$: 9.56, R_p: 6.38					

Table 18: Unit cell parameter and atom parameters resulting from simultaneous refinement of the X-ray data for the 3 h $LiMnPO_4$ samples.

Various reaction time	FWHM (200)	Coherence length [200]	FWHM (020)	Coherence length [020]
3 h LMP samples	0.37 ± 0.03^{o}	21 ± 3 nm	0.35 ± 0.03^{o}	23 ± 3 nm
20 h LMP samples	0.35 ± 0.03^{o}	22 ± 3 nm	0.31 ± 0.03^{o}	25 ± 3 nm

Table 19: The coherence lengths along [200] and [020] directions were calculated for the 3 h $LiMnPO_4$ and the 20 h $LiMnPO_4$ samples respectively.

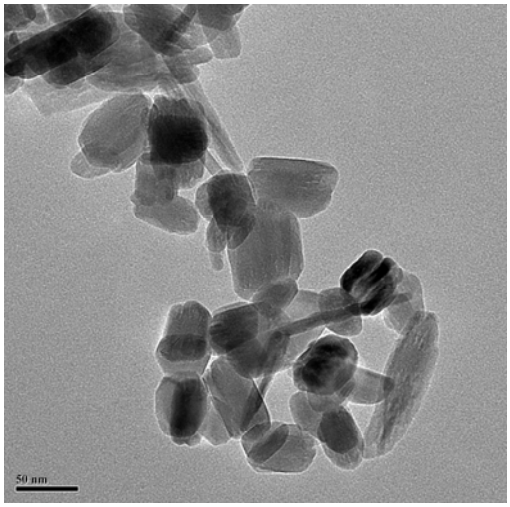

Figure 58: TEM image of the 3 h $LiMnPO_4$ samples.

5.2.4.3 Polyol synthesis of $LiCoPO_4$ nanocrystallites

Synthesis of $LiCoPO_4$ nanocrystallites by polyol process has never been reported before. We employed $Co(OAc)_2$, H_3PO_4, and LiOAc as precursors to see whether we could prepare phase pure samples. Unfortunately, $LiCoPO_4$ was not formed; instead CoO was produced.

$LiCoPO_4$ olivine phase samples were synthesized through two steps. An intermediate was first prepared in polyol process by $Co(OAc)_2$, H_3PO_4 and LiOAc. Additional heat treatment of the intermediate at 650^oC for 0.5 hour or longer yielded $LiCoPO_4$ samples. The corresponding XRD pattern in Figure 59 shows phase pure olivine $LiCoPO_4$ was produced, and the corresponding SEM image in Figure 60 shows a $LiCoPO_4$ sample composed of many rod-shaped particles with 50nm width and up to 200 nm length. The nanocrystalline sizes along [200] and [020] directions were 27 nm and 23 nm, respectively as shown in Table 21, calculated by the Scherrer equation.

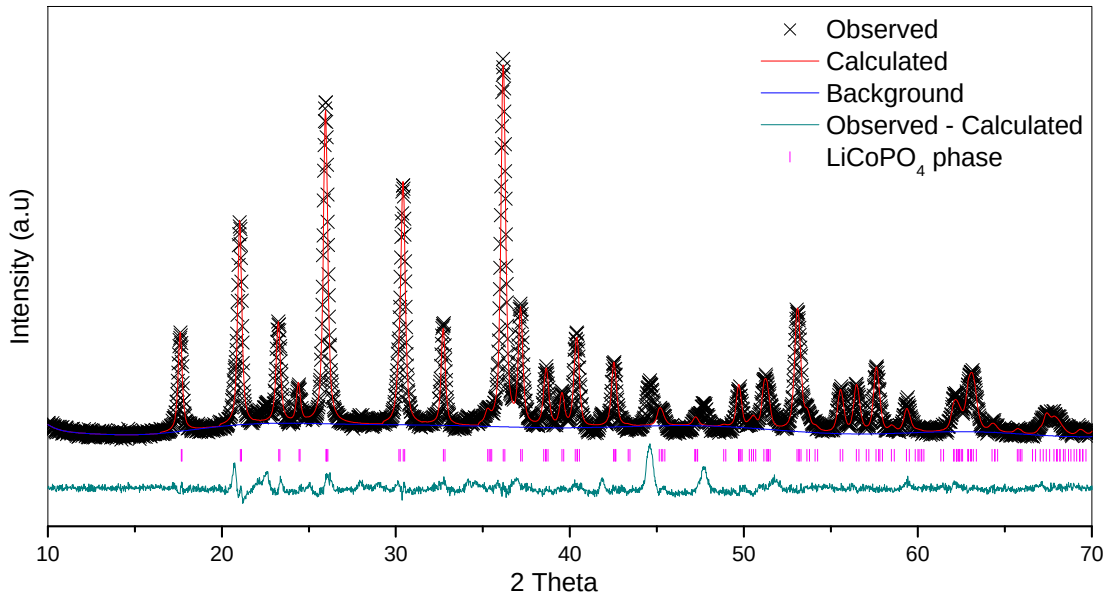

Figure 59: XRD refinement pattern of the 20 h $LiCoPO_4$ samples.

Phase	Atom	Wyck.	x/a, y/b, z/c	$U_{iso}(100Å^2)$	Fraction
Pnma (62)	Li	4a	0,0,0	1.5	1.00
a = 10.218(2) Å	Co	4c	0.2781(2),0.25, 0.9789(7)	3.1(2)	1.00
b = 5.9310(9) Å	P	4c	0.0964(5),0.25,0.422(1)	2.6(2)	1.00
c = 4.7099(7) Å	O1	4c	0.095(1), 0.25, 0.744(2)	2.4(2)	1.00
	O2	4c	0.458(1), 0.25, 0.214(2)	2.4(2)	1.00
	O3	8d	0.1585(8), 0.048(1), 0.272(1)	2.4(2)	1.00
$_wR_p$: 3.95, R_p: 2.73					

Table 20: Unit cell parameter and atom parameters resulting from simultaneous refinement of the X-ray data for the 20 h $LiCoPO_4$ samples.

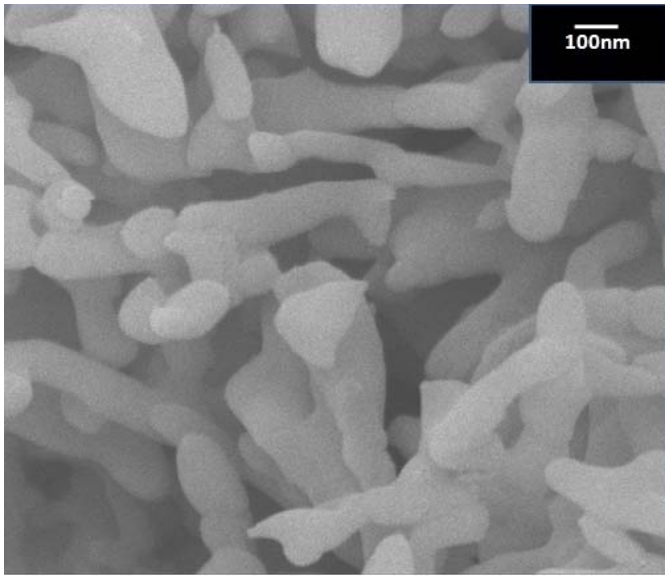

Figure 60: SEM image of the 20 h $LiCoPO_4$ samples.

Condition	FWHM (200)	Coherence length [200]	FWHM (020)	Coherence length [020]
20 h LCP samples	0.29 ± 0.03^o	27 ± 3 nm	0.36 ± 0.03^o	22 ± 3 nm

Table 21: The coherence lengths along [200] and [020] directions were calculated for the 20 h $LiCoPO_4$ samples.

5.2.5 Study of the solid solution properties on Li_xFePO_4 nanocrystallites

5.2.5.1 Temperature-driven solid solution properties of $LiFePO_4$ nanocrystallites

Partially delithiated 20 h $Li_{0.5}FePO_4$ samples was prepared by reacting stoichiometric amounts of $NOBF_4$ and 20 h $LiFePO_4$ samples in 1:2 molar ratio, to study the temperature-driven solid solution properties and size effect. *Ex-situ* XRD measurements were carried out at different temperatures from 100^{o}C to 300^{o}C under a nitrogen atmosphere to drive the formation of the solid solution phase from two-phase (heterosite and triphylite) mixtures. The samples were heated to the desired temperatures and maintained at the same temperatures for 12 hours. They were quenched and measured by XRD at room temperature; those *ex-situ* XRD patterns were shown in Figure 61. It is interesting to see that reduction of the diffraction peaks intensities for both heterosite (red lines in Figure 61) and triphylite (blue lines in Figure 61) was observed when the temperature was 160^{o}C. At the same time, broad diffraction peaks (green lines with arrows at the top in Figure 61) from an intermediate between the reflections of $LiFePO_4$ and $FePO_4$ were also observed. When the temperature increased, the intensities of the broad diffraction peaks increased, which showed a new olivine phase with composition close to $Li_{0.5}FePO_4$. This temperature-driven formation of solid solution phase property was first observed by Delacourt *et al.* in 2005 through the *in-situ* XRD measurement of partially delithiated micron-sized crystallites,[17] and Mössbauer measurements of partially delithiated Li_xFePO_4 ($x \in [0,1]$) samples at various temperatures by Ellis and coworkers.[16] However, a higher transition temperature (i.e. 200^{o}C) was reported.[17] Our results showed that the transition temperature was lower for nanocrystallites, indicating that a lower transition temperature will be required to drive the formation of solid solution phase for smaller nanocrystallites.

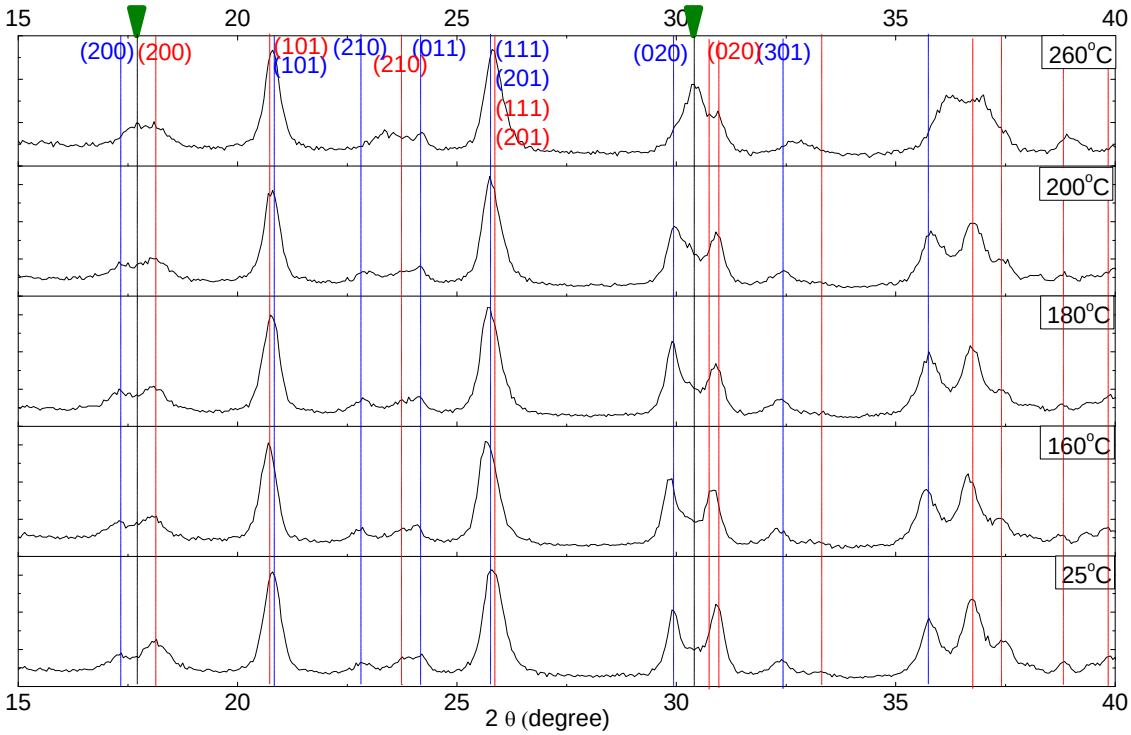

Figure 61: *Ex-situ* XRD patterns of the 20 h $Li_{0.5}FePO_4$ nanocrystallites at 25°C, 160°C, 180°C, 200°C and 260°C; blue lines represent triphylite phase, green line with arrows at the top represent a solid solution phase with composition $Li_{0.5}FePO_4$, and red lines represent heterosite phase.

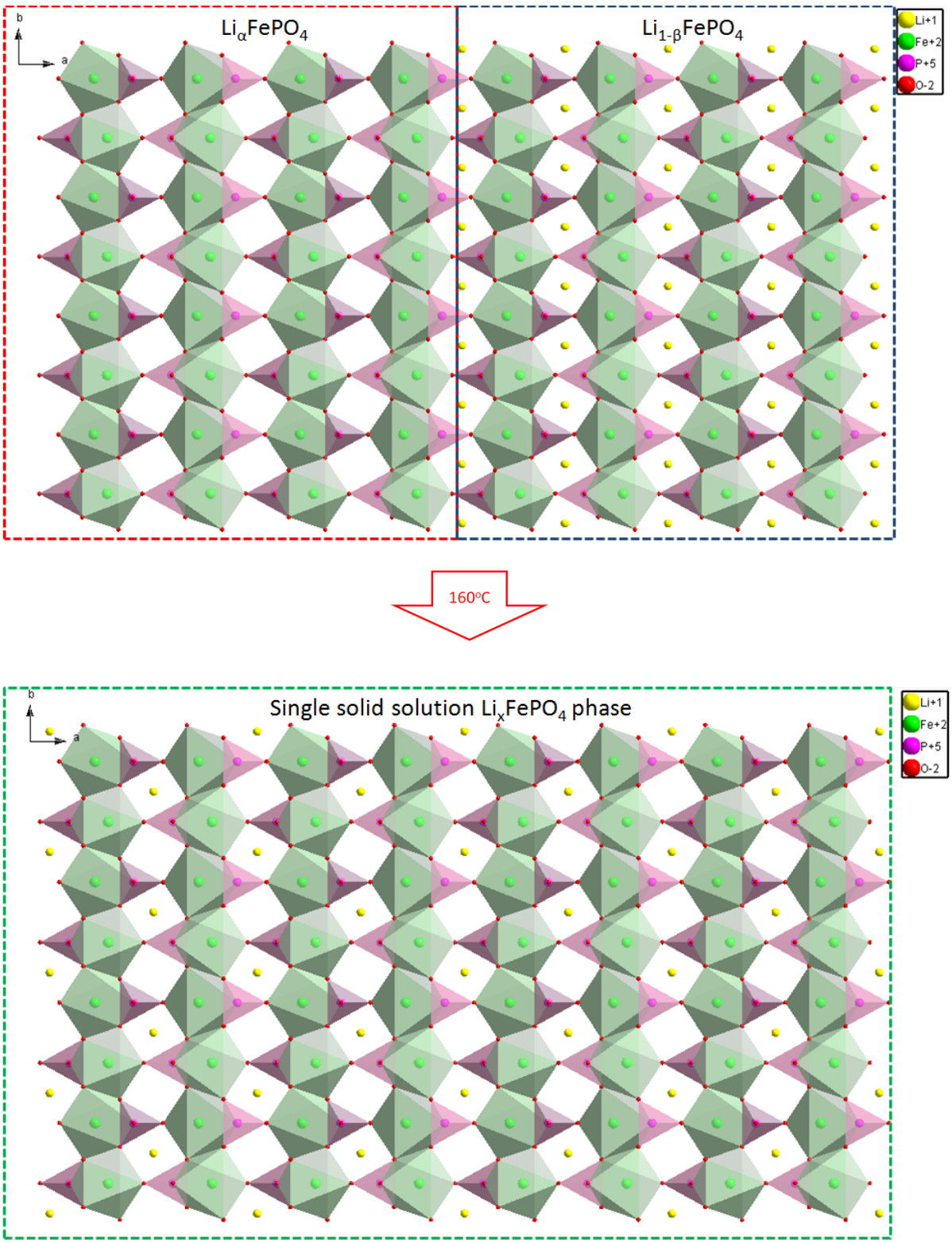

Figure 62: Schematic diagram shows how two-phase mixture observed below 160°C and single solid solution phase observed above 160°C.

To further confirm the above results, another partially delithiated 3 h $Li_{0.5}FePO_4$ samples with smaller crystalline sizes was prepared by reacting stoichiometric amounts of $NOBF_4$ and 3 h $LiFePO_4$ samples in 1:2 molar ratio, to see whether a lower transition temperature could be observed. The smallest dimension of the crystallites we had calculated above was 13.5 nm which was along [200] direction. Surprisingly, heterosite and triphylite phases were not identified clearly from the sample at room temperature. Nonetheless the pattern could easily be indexed as *Pnma* (62) with lattice parameters in between heterosite and triphylite phases shown in Figure 63, suggested that the broad reflection peaks pattern could be composed a single solid solution phase with olivine structure with composition of $Li_{0.5}FePO_4$. However the XRD pattern of 3 h $L_{0.6}FePO_4$ samples could not be indexed as a single phase; triphylite $LiFePO_4$ was also be indexed as a secondary phase. This result suggested that 3 h $Li_{0.5}FePO_4$ samples were composed of more than one phases. Rietveld refinements were used to analyze the XRD patterns of 3 h $L_{0.6}FePO_4$ and 3 h $L_{0.5}FePO_4$ samples. Nonetheless convergent fits could not be obtained due to the broad diffraction peaks in the XRD patterns.

Additional multi-peak fitting procedures in Origin 8.0 were performed on the XRD pattern of 3 h $Li_{0.5}FePO_4$ samples to see if the prepared sample was composted of several phases. In particular the first diffraction peak ((200) plane in SG: *Pnma*) was chosen to study if it was composed of several peaks (diffracted from different phases) as shown in Figure 65. The fitting results in Figure 66 and Figure 67 show that it was very unlikely composed of two phases with different peak positions. On the other hand, it was very likely composed of three peaks with different peak positions. The results provided us an interesting possibility if 3 h $Li_{0.5}FePO_4$ samples contained three phases: a) triphylite $Li_{1-\beta}FePO_4$, b) single solid solution phase with

olivine structure with composition $Li_{0.5}FePO_4$, and c) heterosite $Li_{\alpha}FePO_4$. Nonetheless the results were not strong enough to support the present of those phases. More characterizations, for example Mossbauer measurement of 3 h $Li_{0.5}FePO_4$ samples under different temperatures, have to be conducted to confirm the onset temperature for the formation of solid solution phase.

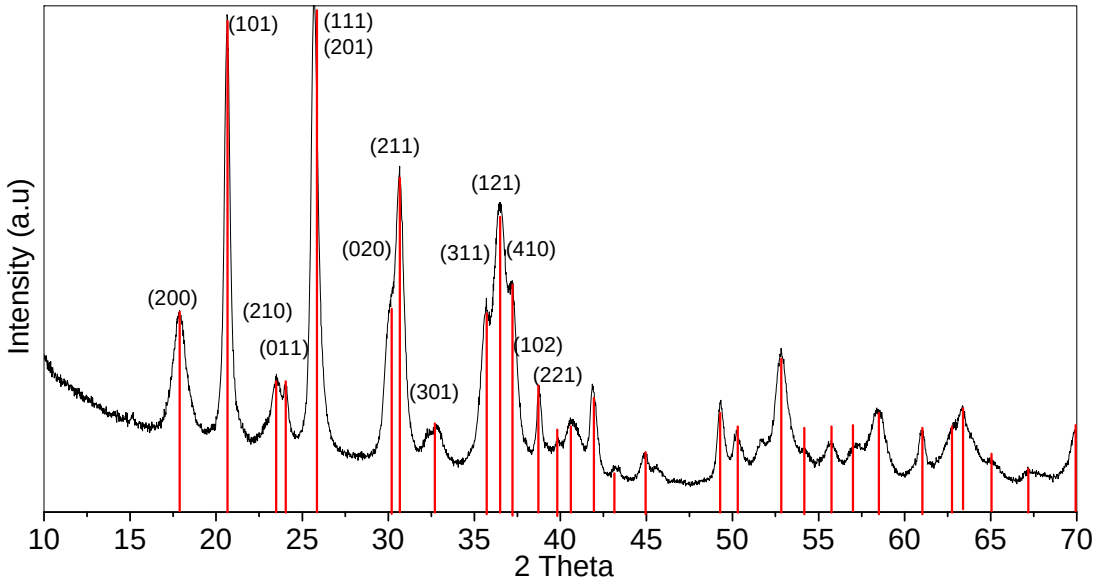

Figure 63: XRD pattern of the 3 h $Li_{0.5}FePO_4$ samples.

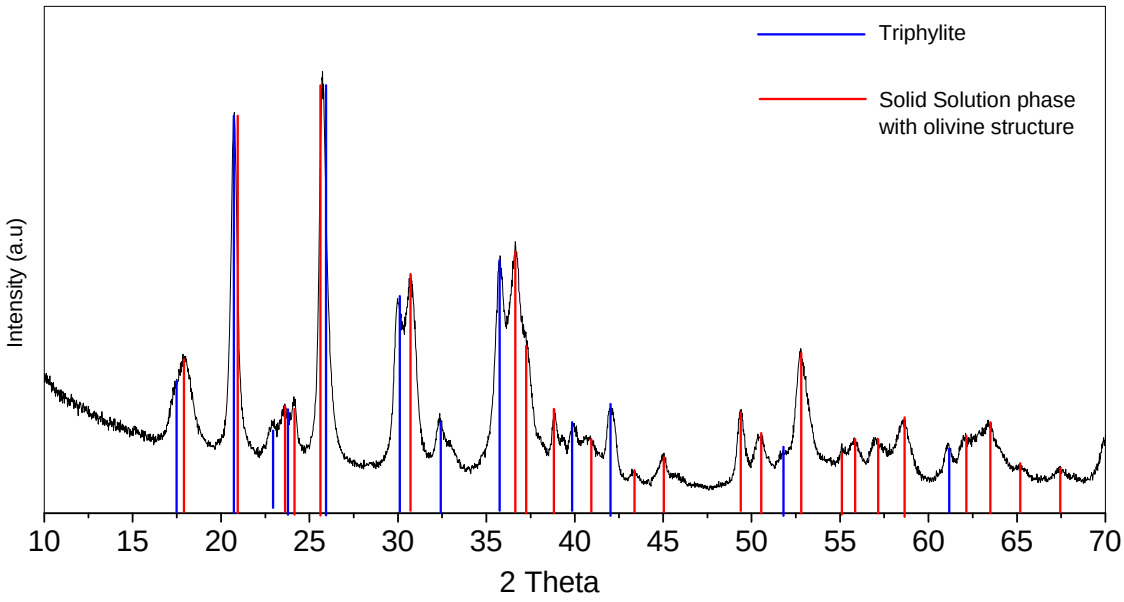

Figure 64: XRD pattern of the 3 h $Li_{0.6}FePO_4$ samples.

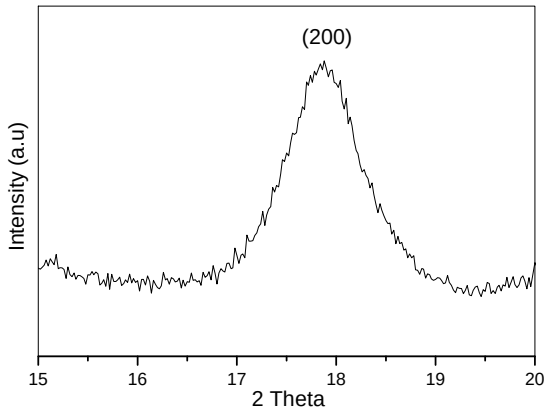

Figure 65: High magnification of the first diffraction peak in the XRD pattern of the 3 h $Li_{0.5}FePO_4$ samples.

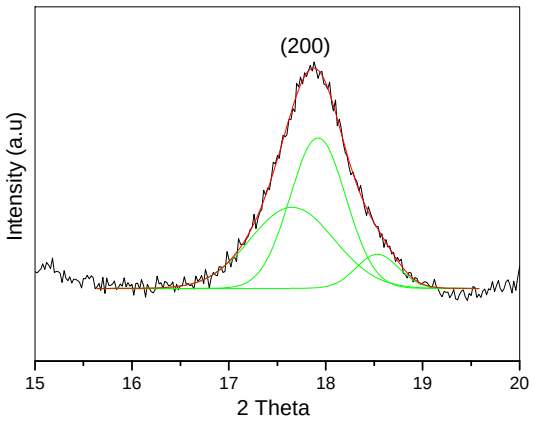

Figure 66: Three-peak fitting of the first diffraction peak in the XRD pattern of the 3 h $Li_{0.5}FePO_4$ samples; R^2 : 0.992.

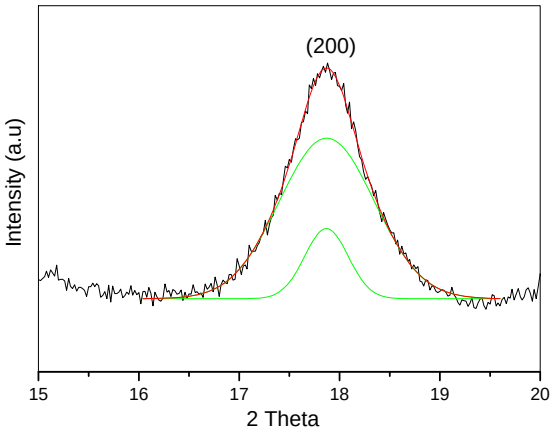

Figure 67: Two-peak fitting of the first diffraction peak in the XRD pattern of the 3 h $Li_{0.5}FePO_4$ samples; R^2 : 0.994.

5.2.4.2 Size-dependent solid solution end members analysis

The electrochemical measurements of the synthesized 20 h $LiFePO_4$ samples were performed by assembling them into CR 2032 coin cells to study the amount of mixed valent intermediate $Li_{\alpha}FePO_4$ and $Li_{1-\beta}FePO_4$ phases which contribute to the lithium ions intercalation reaction in $LiFePO_4$ nanocrystallites. A slow current rate (i.e. C/10) was applied to drive the lithium ions intercalation reactions and minimize the polarization effect so as to address the amount of mixed valent intermediate $Li_{\alpha}FePO_4$ and $Li_{1-\beta}FePO_4$ phases accurately. The voltage profile in Figure 68 indicates about 160 mAh/g (ca. 94% of the theoretical capacity) of reversible capacity was achieved for the first cycle. The reversible capacity was basically contributed from two kinds of lithium (de)intercalation reactions: a) one-phase (de)intercalation reactions, and b) two-phase (de)intercalation reactions.

In principle, when one-phase lithium (de)intercalation reactions occur, the voltage changes with the compositions. The (de)intercalation reactions in that region are shown as below:

Lithium deintercalation reaction of triphylite phase ($LiFePO_4$) to lithium-deficient triphylite phase ($Li_{1-\beta}FePO_4$) occurs in the one-phase region:

$$LiFePO_4 \rightarrow Li_{1-\beta}FePO_4 + \beta Li^+ + \beta e^-$$

Lithium deintercalation reaction of lithium-rich heterosite phase ($Li_\alpha FePO_4$) to heterosite phase ($FePO_4$) occurs in the one-phase region:

$$Li_\alpha FePO_4 \rightarrow FePO_4 + \alpha Li^+ + \alpha e^-$$

Intercalation reaction of lithium-deficient triphylite phase ($Li_{1-\beta}FePO_4$) to triphylite phase ($LiFePO_4$) occurs in the one-phase region:

$$Li_{1-\beta}FePO_4 + \beta Li^+ + \beta e^- \rightarrow LiFePO_4$$

Intercalation reaction of heterosite phase ($FePO_4$) to lithium-rich heterosite phase ($Li_\alpha FePO_4$) occurs in the one-phase region:

$$FePO_4 + \alpha Li^+ + e^- \rightarrow Li_\alpha FePO_4$$

On the other hand, when two-phase lithium (de)intercalation reactions occur, the voltage keeps constant ($\frac{\partial V}{\partial x} = 0$) where 3.45 V vs. Li^+/Li plateau is observed. The (de)intercalation reactions in that region are shown as below:

Lithium deintercalation reaction of lithium-deficient triphylite phase ($Li_{1-\beta}FePO_4$) to lithium-rich heterosite phase ($Li_\alpha FePO_4$) occurs in two-phase region:

$$Li_{1-\beta}FePO_4 \rightarrow Li_\alpha FePO_4 + (1-\beta-\alpha)Li^+ + (1-\beta-\alpha)e^- \quad 3.45 \text{ V vs. } Li^+/Li$$

Lithium intercalation reaction of lithium-rich heterosite phase ($Li_{\alpha}FePO_4$) to lithium-deficient triphylite phase ($Li_{1-\beta}FePO_4$) occurs in two-phase region:

$$Li_{\alpha}FePO_4 + (1-\beta-\alpha)Li^+ + (1-\beta-\alpha)e^- \rightarrow Li_{1-\beta}FePO_4 \quad 3.45 \text{ V vs. } Li^+/Li$$

In principle, the one-phase and two-phase (de)intercalation reaction regions are easily distinguished from their equilibrium voltages; 3.45 V vs. Li^+/Li plateau corresponding to the two-phase region while the other corresponding to the single-phase region. However upon charging and discharging a cell of $LiFePO_4$, there is always a voltage difference between the charge and discharge curve, called the polarization of the cell. The polarization mainly comes from the charge transfer resistance at the interfaces between electrodes and electrolyte. As a result, accurate equilibrium voltage cannot easily be determined. Nonetheless polarization can be minimized at slow current rate.

The voltage-capacity curves in Figure 68 show significant deviations from the plateau voltage at the beginning and end of the charge curve. A similar behaviour was also observed from the discharge curve. Those results indicate that one-phase and two-phase lithium (de)intercalation reactions occur in our 25 X 100 nm $LiFePO_4$ nanocrystallites samples. As described above, cell voltage changes with composition Li_xFePO_4 in the one-phase reactions, while cell voltage keeps constant with composition Li_yFePO_4 in the two-phase reactions. Since the voltage in the voltage profile was not the equilibrium voltage, the amount of solid solution in the end members $Li_{\alpha}FePO_4$ and $Li_{1-\beta}FePO_4$ cannot be estimated accurately. Nonetheless the amount of solid solution contributed from those two end members in our samples was quite similar to in

the 100 nm $LiFePO_4$ nanocrystallites samples observed by Yamada *et al.*[18] Comparing the shapes of our nanocrystallites with *Yamada et al.*,[18] our nanocrystallites were anisotropic with dimension of 25 X 100 nm while the other were isotropic with diameter of 100 – 120 nm. Even through our nanocrystallites have two dimensions that much shorter than 100 nm, no dramatically increment of solid solution from the end members was observed comparing with Yamada *et al.* isotropic 100 nm nanocrystallies. The results suggest the amount of solid solution in the end members at room temperature could be determined by all three dimensions of the nanocrystallies, not particular the shortest one.

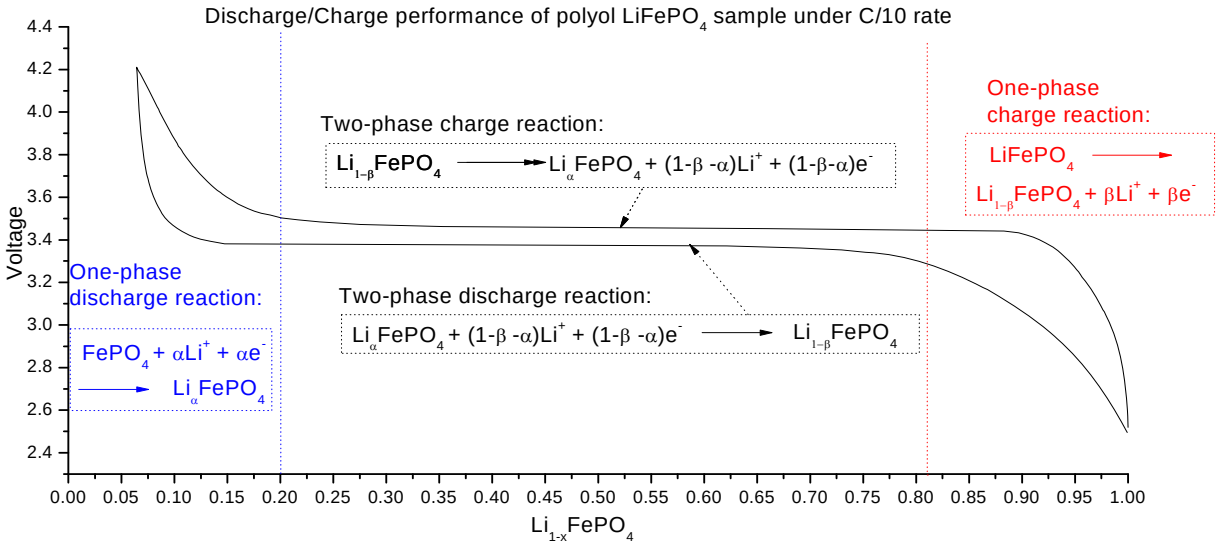

Figure 68: Voltage profile of the polyol 20 h $LiFePO_4$ samples under C/10 current rate.

5.2.6 Study of the solid solutions properties on Li_xMnPO_4 nanocrystallites

Nanocrystallites $Li_{0.5}MnPO_4$ were intended to be prepared through chemical delithiation of $LiMnPO_4$ by NO_2BF_4 in acetonitrile solvent in a glove box. However, the polymer layer which formed on the nanocrystallites in the polyol process reduces the accessibility of the oxidizing agent to the nanocrystallites and the chemical delithiation of the nanocrystallites was not completed after several days of stirring. The delithiated nanocrystallites were later confirmed to be comprised of 84% of $LiMnPO_4$ phase and 16% of $MnPO_4$ phase by XRD-Rietveld refinement.

The as-prepared $Li_{0.84}MnPO_4$ was used to study the temperature-driven solid solution properties by both *in-situ* and *ex-situ* X-ray diffraction measurements. We were interested to study whether solid solution Li_xMnPO_4 ($x \in [0, 1]$) could be stabilized under high temperature conditions in nanocrystalline samples, as we have successfully done for Li_xFePO_4 ($x \in [0, 1]$) nanocrystallies, which has not been reported.

Surprisingly, single solid solution phase Li_xMnPO_4 ($x = 0.84$) cannot be stabilized under high temperature conditions in nanocrystallite samples; the $MnPO_4$ phase was decomposed and converted into $Mn_2P_2O_7$ at 160^oC; complete conversion was observed at 200^oC under an inert gas atmosphere. The result suggests that the $MnPO_4$ phase is thermal instable at high temperature, which could be due to the Jahn-Teller effect in d^4 electronic configuration in Mn^{3+} ions. The corresponding *ex-situ* XRD patterns in Figure 69 show that the $MnPO_4$ phase was completely decomposed at 200^oC under either argon or air atmospheres.

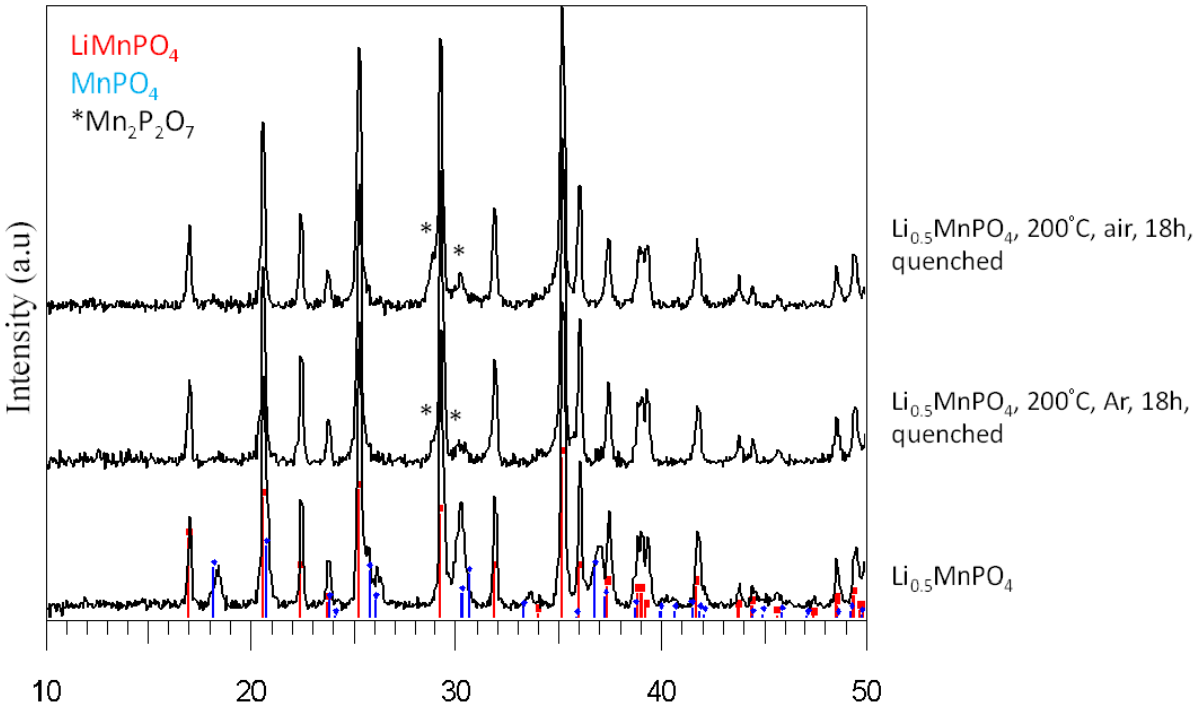

Figure 69: *Ex-situ* XRD patterns of the 20 h $Li_{0.84}MnPO_4$ samples show $MnPO_4$ phase decomposed into $Mn_2P_2O_7$ at elevated temperatures.

Formation of solid solution end members $Li_{\alpha}MnPO_4$ and $Li_{1-\beta}MnPO_4$ has not been reported in nanocrystallites (and bulk crystallites). That could be due to the difficulty on synthesizing pure $LiMnPO_4$ nanocrystallites. It would be interesting to study whether solid solution end members $Li_{\alpha}MnPO_4$ and $Li_{1-\beta}MnPO_4$ can be stabilized under room temperature condition in nanocrystalline samples.

Two-phase $Li_{0.84}MnPO_4$ mixtures were prepared by chemical delithiation of $LiMnPO_4$ by NO_2BF_4 in acetonitrile solvent in a glove box. XRD-Rietveld refinement was performed on the as-prepared $Li_{0.84}MnPO_4$ samples to study the amount of lithium ions in $Li_{\alpha}MnPO_4$ and lithium ions absent in $Li_{1-\beta}MnPO_4$ phases. The refinement result showed a very goodness of fit ($_wR_p$= 3.78; R_p= 3.09) when the triphylite phase $LiMnPO_4$ is fully lithiated and the heterosite phase $MnPO_4$ is fully delithiated, and all of the other parameters are refined. However, convergent fit could not be obtained when the lithium ions occupancy was refined. The above results indicate that large amounts of solid solution in end members $Li_{\alpha}MnPO_4$ and $Li_{1-\beta}MnPO_4$ phases is very unlikely. Therefore, we conclude that $LiMnPO_4$ and $LiMnPO_4$ phases are the only phases present in Li_xMnPO_4 ($x \in [0, 1]$) nanocrystallites. The corresponding XRD-Rietveld refinement in Figure 70 indicates that a very high goodness of fit has been achieved in the $Li_{0.84}MnPO_4$ sample.

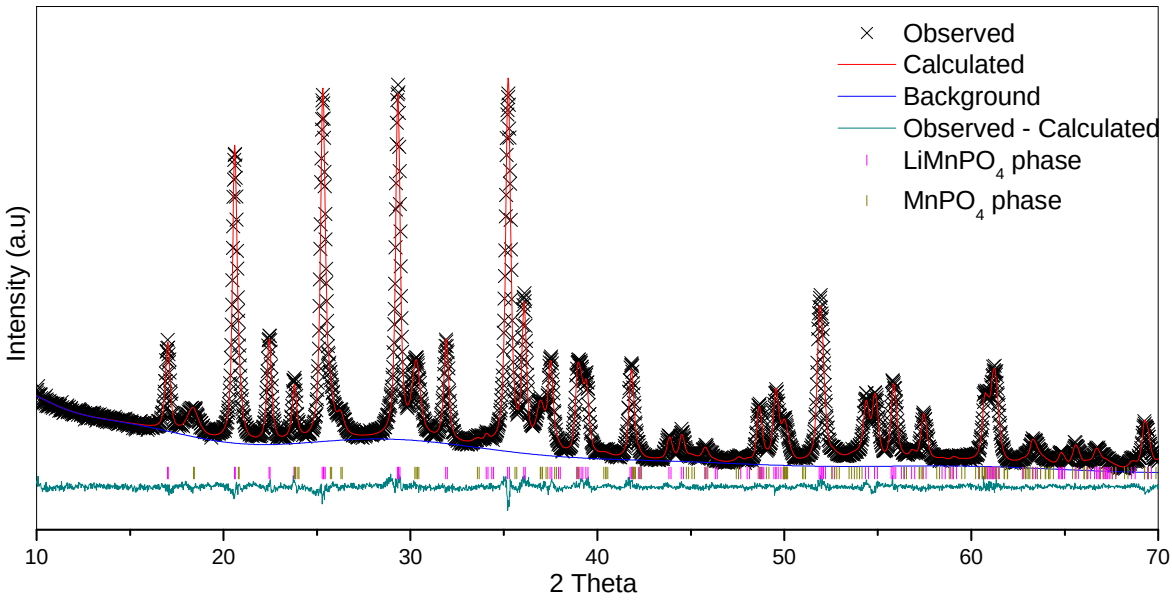

Figure 70: XRD refinement pattern of the 20h $Li_{0.84}MnPO_4$ samples at room temperature.

Phase	Atom	Wyck.	x/a, y/b, z/c	$U_{iso}(100Å^2)$	Fraction
$LiMnPO_4$	Li	4a	0, 0, 0	1.5	1.00
Pnma (62)	Mn	4c	0.2821(1), 0.25, 0.9702(4)	1.89(9)	1.00
a = 10.4476(3) Å	P	4c	0.0929(3), 0.25, 0.4125(5)	2.0(1)	1.00
b = 6.1009(2) Å	O1	4c	0.0930(5), 0.25, 0.7399(9)	1.1(1)	1.00
c = 4.7466(1) Å	O2	4c	0.4555(6), 0.25, 0.2086(9)	1.1(1)	1.00
	O3	8d	0.1596(4), 0.0567(5), 0.2768(6)	1.1(1)	1.00
$MnPO_4$	Mn	4c	0.280(1), 0.25, 0.918(2)	2.2(4)	1.00
Pnma (62)	P	4c	0.098(2), 0.25, 0.387(3)	2.4(7)	1.00
a = 9.661(4) Å	O1	4c	0.163(3), 0.25, 0.682(5)	1.1(1)	1.00
b = 5.917(1) Å	O2	4c	0.453(4), 0.25, 0.166(5)	1.1(1)	1.00
c = 4.773 (1) Å	O3	8d	0.162(3), 0.039(3), 0.231(3)	1.1(1)	1.00
$_wR_p$: 3.78, R_p: 3.09					

Table 22: Unit cell parameter and atom parameters resulting from simultaneous refinement of the X-ray data for the 20 h $Li_{0.84}MnPO_4$ samples.

Chapter 6 Conclusions

Hydrothermal synthesis of $LiFePO_4$ reaction mechanism was studied. Pure tablet $LiFePO_4$ nanocrystallites with 200 nm basal dimensions were prepared by using $NH_4FePO_4 \cdot H_2O$, $LiOH \cdot 2H_2O$ and ascorbic acid in a 4:4:3 molar ratio, typically using a concentration of $NH_4FePO_4 \cdot H_2O$ of 0.133 M. The reagents were placed in an autoclave which was heated at 190^oC for 15 hours. Smaller nanocrystallites were prepared through the careful manipulation of the precursor concentration; 50 nm of nanocrystallites were synthesized at 0.4 M concentration of $NH_4FePO_4 \cdot H_2O$.

Morphology control in $LiFePO_4$ polyol process was studied. $LiFePO_4$ nanocrystalline sizes can be controlled through the careful manipulation of experimental parameters, for example, precursor concentration and reaction time; smaller nanocrystallites can be synthesized at low concentration conditions or for shorter reaction times. $LiFePO_4$ nanorods with various dimensions from 15 X 50 nm to 25 X 100 nm were synthesized. The same reaction procedures and techniques were successfully applied in the fabrication of $LiMnPO_4$ nanocrystallites. Various sizes of $LiMnPO_4$ nanocrystallites from 30 X 50 nm to 50 X 100 nm were synthesized. This thesis is the first to report the synthesis of $LiCoPO_4$ nanocrystallites in a polyol process. $LiCoPO_4$ nanocrystallties with sizes 50 X 200 nm were synthesized.

Solid solution behaviours of Li_xMPO_4 (M = Mn, and Fe) nanocrystallites were studied. The temperature-driven solid solution property of Li_xFePO_4 ($x \in [0, 1]$) was found to be size-dependent, and a lower transition temperature was observed for nanocrystallites than that observed for bulk crystallites. The lowest transition temperature we observed was room

temperature. We have also confirmed that the formation of a solid solution in end members is size-dependent.

Solid solution behaviours in a lithium manganese phosphate system were also studied. However, we were not able to stabilize Li_xMnPO_4 ($x \in [0, 1]$) under high temperatures; the $MnPO_4$ phase decomposed and converted into $Mn_2P_2O_7$ and the XRD-Rietveld refinement of a $Li_{0.84}MnPO_4$ nanocrystalline sample result suggests the amount of solid solution in two end members, $Li_\alpha MnPO_4$ and $Li_{1-\beta}MnPO_4$, was not significant.

Chapter 7 Future directions

Future study will focus on olivine $LiMPO_4$ (M = Ni, and Co) systems. These olivine members have a higher working voltage ($LiNiPO_4$ vs. Li^+/Li = 5.1 V, $LiCoPO_4$ vs. Li^+/Li = 4.8 V) when compared to $LiFePO_4$ which has $LiFePO_4$ vs. Li^+/Li = 3.5 V. We are interested in knowing whether solid solution phases on $Li_\alpha MPO_4$ and $Li_{1-\beta}MPO_4$ end members and full solid solution system Li_xMPO_4 ($x \in [0, 1]$) can be stabilized in nanocrystallites so as to boost the ionic conductivity (or electronic conductivity) for high power and energy applications.

Future studies on doping of $LiMnPO_4$ systems will be conducted to see whether small amounts of dopants (D) in the lattice can sustain the solid solution in $Li_\alpha Mn_{1-y}D_yPO_4$ and $Li_{1-\beta}Mn_{1-y}D_yPO_4$ end members and full solid solution system $Li_xMn_{1-y}D_yPO_4$ ($x \in [0, 1]$). We have reported that solid solution behaviours cannot be sustained in either end members or under high temperature conditions for Li_xMnPO_4 ($x \in [0, 1]$) nanocrystallites. We are interested in learning whether small amounts of dopants (D) in the lattice can minimize the volume change and stabilize the solid solution behaviours.

Further studies on the synthesis of substoichiometry of olivine $LiMPO_4$ (M = Mn, Fe, Co, and Ni) will be carried out to see whether small amounts of defects can be created during the reaction and stabilize the solid solution behaviour. Masquelier *et al*. recently reported that they have synthesized defected lithium iron phosphate at a relatively low temperature condition,

maintaining a full solid solution behaviour at room temperature during cell discharge/charge.[1] Even though the origin of the solid solution behaviour is not understood, it provides additional parameters, such as defect, particle size and temperature, for chemists and material scientists to control the solid solution system.

References

Chapter 1

[1] Ip C. C. D. Putrid Air Puts Heath At Risk: How to cope with it. *Improving Hong Kong* [online] **2006**, *3*, 4.

[2] World Health Organization (WHO) Air quality guidelines for particulate matter, ozone, nitrogen dioxide and sulfur dioxide - Global update 2005 - Summary of risk assessment.

[3] Alternative Fuels & Advanced Vehicles Data Center, Energy Efficiency and Renewable Energy, U.S. Department of Energy, Tables 6.2 and 4.34 in GREET 1.5 Transportation Fuel-Cycle Model.

[4] Tarascon J.-M.; Armand M. *Nature*, **2001**, *414*, 359.

[5] Canadian Consumer Battery Baseline Study, Final Report, Environment Canada, February 2007.

[6] US Department of Transportation, Bureau of Transportation Statistics, Omnibus Household Survey Volume 3, Issue 4, October 2003.

[7] Nazri G.-A.; Pistoia G. *Chapter 21 Lithium-ion batteries for EV, HEV and other industrial application, Lithium Batteries*, Kluwer Academic Publishers 2004.

Chapter 2

[1] Nazri G. A.; Pistoia G. *Lithium Batteries Science and Technology,* 1st ed., Kluwer Boston, Inc., 2004, p. 3.

[2] Whittingham M. S.; Xiao J.; Quan F.; Chen J.; Wang S.; Chernova N. *ECS Cancun* 2006

[3] Takahashi M.; Ohtsuka H.; Akuto K.; Sakurai Y. *J. Electrochem. Soc.* **2005**, 152(5), A899.

[4] Santoro R. P. ; Newnham R. E. *Acta Cryst.* **1967**, *22*, 344.

[5] Yang S.; Zavalij P. Y.; Whittingham M. S. *Electrochem. Comm.* **2001**, *3,* 505.

[6] Chen J.; Whittingham M. S. *Electrochem. Comm.* **2006**, *8*, 855.

[7] Ellis B.; Kan W. H.; Makahnouk W. R. M.; Nazar L. F. *J. Mate. Chem.* **2007**, *17*, 3248.

[8] Croce F.; D'Epifanio A.; Hassoun J.; Deptula A.; Olczac T.; Scrosati B. *Electrochem. Solid-state Lett.* **2002**, 5 (3), A47.

[9] Hu Y.; Doeff M. M.; Kostecki R.; Finõnes R. *J. Electrochem. Soc.* **2004**, 151 (8), A1279.

[10] Dominko R.; Bele M.; Gaberscek M.; Remskar M.; Hanzel D.; Pejovnik S.; Jamnik J. *J. Electrochem. Soc.* **2005**, 152 (3), A607.

[11] Park K. S.; Son J. T.; Chung H. T.; Kim S. J.; Lee C. H.; Kim H. G. *Electrochem. Comm.* **2003**, 5 (10) 839.

[12] Arnold G.; Garche J.; Hemmer R.; Strobele S.; Volger C.; Wohlfahrt-Mehrens M. *J. Power Sources* **2003**, *119-121*, 247.

[13] Kim D. H.; Kim J. *Electrochem. Solid-state Lett.* **2006** 9 (9), 1439.

[14] Kim D. H.; Kim T. R.; Im J. S.; Kang J. W.; Kim J. *Physica Scripta* **2007**, *T129,* 31.

[15] Kim D. H.; Kim J. *J. Phys. Chem. Solids* **2007**, *68*, 734

[16] Streltsov V. A.; Belokoneva E. L.; Tsirelson V. G.; Hansen N. K. *Acta Cryst.* **1993**, *B49*, 147.

[17] Padhi A.K.; Nanjundaswamy K. S.; Goodenough J. B. *J. Electrochem. Soc.* **1997**, 144(4), 1188.

[18] Paclh A. K.; Nanjunclaswam K. S.; Masquelier C.; Okada S.; Gooclenough J. B. *J. Electrochem. Soc.* **1997**, 144 (5), 1609.

[19] Yamada A.; Chung S. C.; Hinokuma K. *J. Electrochem. Soc.* **2001**, 148 (3), A224.

[20] Ouyang C.; Shi S.; Wang Z.; Huang X.; Chen L. *Phys. Rev. B* **2004**, *69*, 104303.

[21] Morgan D.; Van der Ven A.; Ceder G. *Electrochem. Solid-State Lett.* **2004**, 7 (2), A30.

[22] Nishimura S. I.; Kobayashi G.; Ohoyama K.; Kanno R.; Yashima M.; Yamada A. *Nat. Mater.* **2008**, 7(9), 707.

[23] Li J.; Yao W.; Martin S.; Vaknin D. *Solid State Ionics* **2008**, *179*, 2016.

[24] Amin R.; Balaya P.; Maier J. *Electrochem. Solid-State Lett.* **2007**, 10 (1), A13.

[25] Maier J.; Amin R. *J. Electrochem. Soc.* **2008**, 155 (4), A339.

[26] Amin R.; Maier J.; Balaya P.; Chen D. P.; Lin C. T. *Solid State Ionics* **2008**, *179*, 1683.

[27] Formin V. I.; Genezdilov V. P.; Kurnosov V. S.; Peschanskii A. V.; Yeremenko A. V.; Schmid H.; Rivera J.-P.; Gentil S. *Low Temp. Phys.* **2002**, *28*, 203.

[28] Chen G.; Song X.; Richardson T. J. *Electrochem. Solid-State Lett.* ***2006***, 9 (6), A295.

[29] Laffont L.; Delacourt C.; Gibot P.; Wu M. Y.; Kooyman P.; Masquelier C.; Tarascon J. M. *Chem. Mater.* **2006**, *18,* 5520.

[30] Anderrson A. S.; Thomas J. O.; Kalska B.; Haggstrom L. *Electrochem. Solid-State Lett.*, **2000**, 3 (2), 66.

[31] Huang H.; Yin S. C.; Nazar L. F. *Electrochem. Solid-State Lett.* **2001**, 4 (10), A170.

[32] Ravet N.; Chouinard Y.; Magan J. F.; Besner S.; Gauthier M.; Armand M. *J. Power Sources* **2001**, *97-98*, 503.

[33] Bruce P. *Materials for Lithium Batteries: Is small beautiful?* The Seventh International Symposium on Electrochemical Micro & Nano-system Technologies, Ein Gedi, Israel ,16 September, 2008

[34] Chung S. Y.; Bloking J. T.; Chiang Y. M. *Nat. Mater.* **2002**, 1(2), 123.

[35] Smart L. E.; Moore E. A. Solid State Chemistry An Introduction, 3rd ed.; CRC Press Taylor & Francis Group, 2005; p. 104.

[36] Ravet N.; Abouimrane A.; Armand M. Nat. Mater. **2003**, 2(11), 702.

[37] Herle P. S.; Ellis B.; Coombs N.; Nazar L. F. *Nat. Mater.* **2004**, 3(3), 147.

[38] Wagemaker M.; Ellis B. L.; Lützenkichen-Hecht D.; Mulder F. M.; Nazar L. F. *Chem. Mater.* **2008**, *20*, 6313.

[39] Delacourt C.; Poizot P.; Tarascon J. M.; Masquelier C. *Nat. Mater.* **2005**, 4(3), 254.

[40] Ellis B.; Perry L. K.; Ryan D. H.; Nazar L. F. *J. Am. Chem. Soc.* **2006**, *128*, 11416.

[41] Yamada A.; Koizumi H.; Nishimura S. I.; Sonoyama N.; Kanno R.; Yonemura M.; Nakamura T.;

Kobayashi Y. *Nat. Mater.* **2006**, *5*, 357.

[42] Meethong N.; Huang H. Y. S.; Carter W. C.; Chiang Y. M. *Electrochem. Solid-State Lett.* **2007**, 10 (5), A134.

[43] Gibot P.; Casas-Cabanas M.; Laffont L.; Levasseur S.; Carlach P.; Hamelet S.; Tarascon J.- M.; Masquelier C. *Nat. Mater.* **2008**, *7*, 741.

[44] Delmas C.; Maccario M.; Croguennec L.; Cras F. L.; Weill F. *Nat. Mater.* **2008**, *7*, 665.

[45] Gopalakrishnan J. *Chem. Mater.* **1995**, 7 (7), 1265.

[46] Norquist A. J.; O'Hare D. *J. Am. Chem. Soc.* **2004**, *126*, 6673.

[47] Centi G.; Perathoner S.; Trifiro F.; Aboukais A.; Aissi C. F.; Guelton M. *J. Phys. Chem.* **1992**, *96* (6), 2617.

[48] Corma A.; Nazarro M. T.; Pariente J. P. *J. Chem. Soc., Chem. Comm.* **1994**, *2*, 147.

[49] Cambolor M. A.; Corma A.; Martinez A.; Perezpariente J. *J. Chem. Soc., Chem. Comm.* **1992**,

8, 589.

[50] Dobley A.; Ngala K.; Yang S. F.; Zavalij P. Y.; Whittingham M. S. *Chem. Mater.* **2001**, 13 (11), 4382.

[51] Aoki K.; Kusakabe K.; Morooka S. *J. Membrane Sci.* **1998**, 141 (2), 197.

[52] Zheng Y. Q.; Shi E. R.; Chen Z. Z.; Li W. J.; Hu X. F. *J. Mater. Chem.* **2001**, 11 (5) 1547.

[53] Hirano M.; Kato E. *J. Am. Ceram. Soc.* **1996**, 79 (3), 777.

[54] Chen S. F.; Yu S. H.; Yu B.; Ren L.; Yao W. T.; Colfen H. *Chem.- Eur. J.* **2004**, 10 (12), 3050.

[55] Lin C. F.; Hsi H. C. *Environ. Sci. Technol.* **1995**, 29 (4), 1109.

[56] Kanamura K.; Koizumi S. H.; Dokko K. R. *J. Mater. Sci.* **2008**, 43 (7), 2138.

[57] Fievet F.; Lagier J. P.; Blin B.; Beaudoin B.; Figlarz M. *Solid State Ionics* **1989**, *32-3*, 198.

[58] Saravanan P.; Jose T. A.; Thomas P. J.; Kulkarni G. U. *B. Mater. Sci.* **2001**, 24 (5), 515.

[59] Hinotsu T.; Jeyadevan B.; Chinnasamy C. N.; Shinoda K.; Tohji K. *J. App. Phys.* **2004**, 95 (11), 7477.

[60] Kurihara L. K.; Chow G. M.; Schoen P. E. *Nanostruct. Mater.* **1995**, 5 (6), 607.

[61] Ho C. M.; Yu J. C.; Kwong T.; Mak A. C.; Lai S. Y. *Chem. Mater.* **2005**, 17 (17), 4514.

[62] Palchik O.; Kerner R.; Gedanken A.; Weiss A. M.; Slifkin M. A.; Palchik V. *J. Mater. Chem.* **2001**, 11 (3), 874.

Chapter 5

[1] Yang S.; Zavalij P. Y.; Whittingham M. S. *Electrochem. Comm.* **2001**, *3*, 505.

[2] Kokko K.; Koizumi S.; Nakano H.; Kanamura K. *J. Mater. Chem.* **2007**, 17 (45), 4803.

[3] Kim D. H.; Kim J. *Electrochem. Solid-State Lett.* **2006**, 9 (9) A439.

[4] Delacourt C.; Poizot P.; Levasseur S.; Maquelier C. *Electrochem. Solid-State Lett.* **2006**, *9*, A352.

[5] Barker J.; Saidi M. Y.; Swoyer J. L. *Electrochem. Solid-State Lett.* **2003**, *6*, A53.

[6] Ellis B.; Kan W. H.; Makahnouk W. R. M.; Nazar L. F. *J. Mater. Chem.* **2007**, *17*, 3248.

[7] Chen J.; Vacchio M. J.; Wang S.; Chernova N.; Zavalij P. Y.; Whittingham M. S. *Solid State Ionics* **2008**, *8*, A409.

[8] Vassilous J. K.; Mehrotra V.; Russell M. W.; Giannelis E. P.; McMichael R. D.; Shull R. D.; Ziolo R. F. *J. App. Phys.* **1993**, *73*, 5109.

[9] Lopes I.; Hassan N. E.; Guerba H.; Wallez G.; Davidaon A. *Chem. Mater.* **2006**, *18*, 5826.

[10] Gibot P.; Casas-Cabanas M.; Laffont L.; Levasseur S.; Carlach P.; Hamelet S.; Tarascon J.- M.; Masquelier C. *Nat. Mater.* **2008**, *7*, 741.

[11] Chen J.; Whittingham M. S. *Electrochem. Comm.* **2006**, *8*, 855.

[12] Chen J.; Vacchio M. J.; Wang S.; Chernova N.; Zavalij P. Y.; Whittingham M. S. *Solid State Ionics* **2008**, *178*, 1676.

[13] Padhi A. K.; Najundaswamy K. S.; Goodenough J. B. *J. Electrochem. Soc.* **1997**, 144 (4), 1188.

[14] Anderson A. S.; Thomas J. O. *J. Power Sources* **1999**, 81, 463.

[15] Kim T. R.; Kim D. H.; Ryu H. W.; Moon J. H.; Lee J. H.; Boo S.; Kim J. *J. Phys. Chem. Solids* **2007**, *68*, 1203.

[16] Ellis B.; Perry L. K.; Ryan D. H.; Nazar L. F. *J. Am. Chem. Soc.* **2006**, *128*, 11416.

[17] Delacourt C.; Poizot P.; Tarascon J.-M.; Masquelier C. *Nat. Mater.* **2005**, *4*, 254.

[18] Yamada A.; Koizumi H.; Nishimura S. I.; Sonoyama N.; Kanno R.; Yonemura M.; Nakamura T.; Kobayashi Y. *Nat. Mater.* **2006**, *5*, 357.

Chapter 7

[1] Gibot P.; Casas-Cabanas M.; Laffont L.; Levasseur S.; Carlach P.; Hamelet S.; Tarascon J.-M.; Masquelier C. *Nat. Mater.* **2008**, *7*, 741.